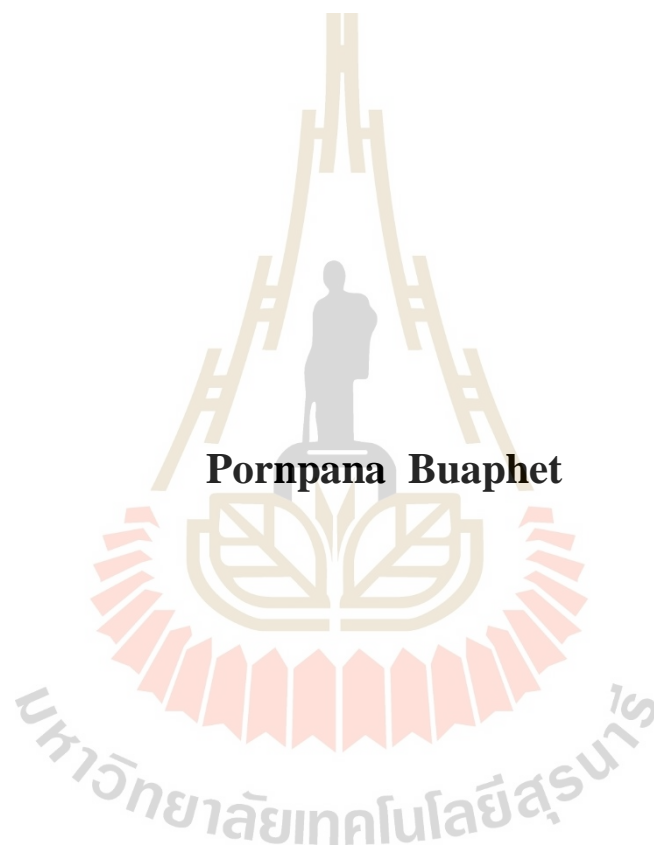


**LOW-TEMPERATURE ELECTRONIC STRUCTURE OF
TWO-DIMENSIONAL ELECTRON GAS AT THE
SURFACE OF La-DOPED SrTiO₃(110)**



**A Thesis Submitted in Partial Fulfillment of the Requirements for the
Degree of Doctor of Philosophy in Physics
Suranaree University of Technology
Academic Year 2015**

โครงสร้างอิเล็กทรอนิกส์ที่อุณหภูมิต่ำของแก๊สอิเล็กตรอนสองมิติบนพื้นผิว
สตรอนเทียมไททานตที่ถูกเจือด้วยแลนทานัม ในระนาบผลึก (110)

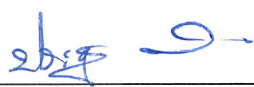


วิทยานิพนธ์นี้เป็นส่วนหนึ่งของการศึกษาตามหลักสูตรปริญญาวิทยาศาสตรดุษฎีบัณฑิต
สาขาวิชาฟิสิกส์
มหาวิทยาลัยเทคโนโลยีสุรนารี
ปีการศึกษา 2558

**LOW-TEMPERATURE ELECTRONIC STRUCTURE OF
TWO-DIMENSIONAL ELECTRON GAS AT THE
SURFACE OF La-DOPED SrTiO₃(110)**

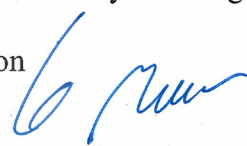
Suranaree University of Technology has approved this thesis submitted in partial fulfillment of the requirements for the Degree of Doctor of Philosophy.

Thesis Examining Committee



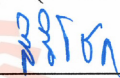
(Assoc. Prof. Dr. Prayoon Songsiriritthigul)

Chairperson



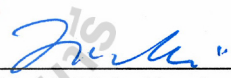
(Assoc. Prof. Dr. Worawat Meevasana)

Member (Thesis Advisor)




(Assoc. Prof. Dr. Sirichok Jungthawan)

Member



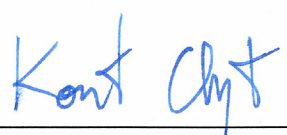
(Dr. Hideki Nakajima)

Member




(Dr. Narong Chanlek)

Member



(Assoc. Prof. Flt. Lt. Dr. Kontorn Chamnprasart)



(Assoc. Prof. Dr. Worawat Meevasana)

Vice Rector for Academic Affairs
and Internationalization

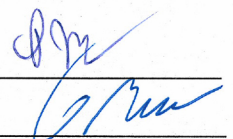
Dean of Institute of Science

กรพณา บัวเพชร : โครงสร้างอิเล็กทรอนิกส์ที่อุณหภูมิต่ำของแก๊สอิเล็กตรอนสองมิติบน
พื้นผิวสตรอนเทียมไททานेटที่ถูกเจือด้วยแลนทานัม ในระนาบผลึก (110) (LOW-
TEMPERATURE ELECTRONIC STRUCTURE OF TWO-DIMENSIONAL
ELECTRON GAS AT THE SURFACE OF La-DOPED SrTiO₃(110)).
อาจารย์ที่ปรึกษา : รองศาสตราจารย์ ดร.วรวัดน์ มีวาสนา, 81 หน้า.

งานวิจัยนี้ได้ทำการศึกษาโครงสร้างอิเล็กทรอนิกส์บนพื้นผิวสตรอนเทียมไททานेटที่ถูก
เจือด้วยแลนทานัมในระนาบผลึก (110) โดยใช้เทคนิคโฟโตอิมิตชันแบบแยกแยะเชิงมุม โดยใน
ระหว่างการทดลอง วัสดุตัวอย่างจะถูกลอกชั้นผิวที่ความดันต่ำกว่า 10^{-11} ทอร์และที่อุณหภูมิ 20 K
เพื่อคงความสะอาดของผิวหน้าของวัสดุ รายละเอียดโครงสร้างทางอิเล็กทรอนิกส์ของวัสดุที่บริเวณ
กึ่งกลางของโครงสร้าง (Γ point of the 2nd-Brillouin zone) ถูกศึกษาโดยใช้แสงที่มีโพลาไรเซชัน
ขนานและตั้งฉากกับพื้นผิวและศึกษาเกี่ยวกับผลของการฉายแสงอัลตราไวโอเล็ต (UV) บนพื้นผิว
สตรอนเทียมไททานेटด้วยพลังงานโฟตอน 50 อิเล็กตรอน โวลต์ (eV) และความเข้มแสง 3.5 นาโน
แอมแปร์ (nA) ผลการทดลองพบว่าแก๊สอิเล็กตรอนสองมิติ (2DEGs) มีการก่อดับนพื้นผิว
สตรอนเทียมทันทีที่มีการลอกชั้นผิว ซึ่งสามารถคำนวณหาความหนาแน่นของประจุได้ประมาณ
 2.34×10^{14} ต่อตารางเซนติเมตร (cm²) นอกจากนี้ยังพบสถานะในช่องว่างพลังงาน (in-gap state)
ที่มีพลังงานยึดเหนี่ยว (binding energy) ประมาณ 1.1 อิเล็กตรอน โวลต์ (eV) จากการศึกษาการ
กระจายตัวของแถบพลังงาน (band dispersion) และพื้นผิวเฟอร์มี (Fermi surface map) พบว่าวัสดุ
ชนิดนี้แสดงสมบัติแบบแอนไอโซทรอปิกในระนาบผลึกทิศทางต่างกัน โดยพบแถบพลังงาน 3
แถบ เรียกว่า heavy, semi-heavy และ lightly bands ในทิศทาง [001] หรือ k_z ซึ่งสามารถหามวลยัง
ผล (effective mass, m^*) ได้ดังนี้คือ $m^* \cong 10m_e$, $m^* \cong 1.5m_e$ และ $m^* \cong 0.35m_e$ ตามลำดับ เมื่อ
 m_e คือมวลของอิเล็กตรอน ส่วนในทิศทาง [110] หรือ k_x สังเกตเห็นแถบพลังงานเพียง 2 แถบ ซึ่งมี
ค่า $m^* \cong 5m_e$ และ $m^* \cong 0.35m_e$ โดยผลจากสมบัติแอนไอโซทรอปิกที่ค้นพบนี้บ่งชี้ว่าพื้นผิวของ
วัสดุสตรอนเทียมไททานेटที่ถูกเจือด้วยแลนทานัม ในระนาบผลึก (110) จะมีค่าสัมประสิทธิ์ซีเบค
ที่สูงซึ่งมีโอกาสด้อยอดและพัฒนาเพื่อนำไปใช้เป็นวัสดุเทอร์โมอิเล็กทริกได้ ยิ่งไปกว่านั้นจาก
การศึกษาค่าความหนาแน่นของประจุบนผิวบ่งชี้ว่าพื้นผิวสตรอนเทียมไททานेटที่ถูกเจือด้วยแลน
ทานัมในระนาบผลึก (110) มีโอกาสที่จะแสดงสมบัติเฟอร์โรแมกเนติก

สาขาวิชาฟิสิกส์
ปีการศึกษา 2558

ลายมือชื่อนักศึกษา
ลายมือชื่ออาจารย์ที่ปรึกษา



PORNPANA BUAPHET : LOW-TEMPERATURE ELECTRONIC
STRUCTURE OF TWO-DIMENSIONAL ELECTRON GAS AT THE
SURFACE OF La-DOPED SrTiO₃(110). THESIS ADVISOR :
ASSOC. PROF. WORAWAT MEEVASANA, Ph.D. 81 PP.

ELECTRONIC STRUCTURE/TWO-DIMENSIONAL ELECTRON GAS/
SrTiO₃(110)

In this thesis, the electronic structure of La-doped SrTiO₃(110) surface has been studied using Angle-Resolved Photoemission (ARPES). Samples were cleaved in ultra high vacuum (UHV) with pressure better than 10⁻¹¹ torr at temperature of 20 K to obtain high purity surface. The detailed electronic structures focusing at the zone centre (Γ -point) of the second Brillouin zone were studied by horizontal and vertical polarization of light as a function of UV irradiation (exposure to 50 eV ultraviolet light with intensity of 3.5 nA). The two-dimensional electron gases (2DEGs) were observed on a polar surface of La-doped SrTiO₃(110) with the density as large as 2.34 $\times 10^{14}$ cm⁻² right after cleaving the surface. The in-gap state (1.1 eV binding energy) was observed increasingly as a function of light dosing. By studying the band dispersion and Fermi surface map (FSM), we found that effective masses of this sample exhibit anisotropic behavior in different crystallographic directions. The results showed at least 3 ellipsoid bands along k_Z or [001]-direction indicated as heavy, semi-heavy and lightly bands with effective masses (m^*) to be around 10, 1.5, 0.35 of the electron masses (m_e) respectively. The heavy ($m^* \cong 5m_e$) and lightly ($m^* \cong 0.35m_e$) bands were observed along k_M or [1 $\bar{1}$ 0]-direction. The contribution of

various anisotropic effective masses indicates that $\text{SrTiO}_3(110)$ may have a high Seebeck coefficient which can be used for thermoelectric application. Moreover, ferromagnetism is expected to occur at the surface of $\text{SrTiO}_3(110)$ as well.



School of Physics

Academic Year 2015

Student's Signature _____

Advisor's Signature _____

ACKNOWLEDGEMENTS

First of all, I would like to express my gratitude to my research advisor, Asst. Prof. Dr. Worawat Meevasana, for his guidance, assistance and encouragement. He is very kind and advises me to solve both of the experimental and my personal problems. This research project would not have been possible without him.

I would like to acknowledge Assoc. Prof. Dr. Prayoon Songsiriritthigul, Assoc. Prof. Dr. Sirichok Jungthawan, Dr. Hideki Nakajima, and Dr. Narong Chanlek, thesis defense committee, for giving their valuable time to listen to me and guiding good research aspects for my thesis defense.

I would like to thank the members of Meevasana group; Mr. Tanachat Eknapakul, Mr. Sanit Suwanwong, Mr. Jirapat Kullapapinyokul, Mr. Sumeth Siroj, Mr. Sarawudh Nathabamroong, Dr. Chivalrat Masingboon, and Dr. Panupong Jaiban. They are very kind and always give me fun while doing the experiment. I am grateful to all members in this group who shared with me many tips and tricks in both the experimental and computational work of this research project, making my research and education experience more pleasant. Especially, Mr. Tanachat Eknapakul, thank for his guidance in using IGOR, LATEX, and other programs used in this research. He is very kind and always supports me when I need some helps. Despite, I cannot forget to thank Dr. Panupong Jaiban for taking me to the hospital for 2-3 months continuously when I got sick and had an accident. At that time, he also helped me for picking my son to go and back from school every day.

I would like to thank Mr. Wisit Paewkratok and Mr. Thiti Sutthivong who taught me the basics of the LabVIEW program for controlling the cryostat system.

I would like to thanks Dr. Sung Kwan Mo, the beamline scientist at Advanced Light Source (USA) for the facility while doing ARPES measurement.

I am thankful to Dr. Philip King in School of Physics and Astronomy, University of St Andrews and Dr. Mohammad Saeed Bahramy in the department of Applied Physics, The University of Tokyo who helped me to calculate the band spectrum in this thesis.

I would like to thanks all staffs and students at the school of Physics, SUT, especially Mrs. Phengkhae Phetmai for her helps in document.

I am also thankful to Dr. Sampart Cheedket. He is both of my friend and my brother who took care of me and my son for staying with him about 2 years before I had a residence when I was studying at SUT.

Importantly, I would like to acknowledge the ministry of science and technology, Thai government, for financial supports.

Last but not least, I would like to extend my deepest gratitude to my family and friends, especially my son (Thepnarin Buaphet), who always encourage and stand beside me all situations. Without their continued support and encouragement, I would not have been able to make it this far. Thank you for having faith in me.

Pornpana Buaphet

CONTENTS

	Page
ABSTRACT IN THAI.....	I
ABSTRACT IN ENGLISH	II
ACKNOWLEDGEMENTS	IV
CONTENTS.....	VI
LIST OF TABLES	IX
LIST OF FIGURES.....	X
LIST OF ABBREVIATIONS.....	XIX
CHAPTER	
I INTRODUCTION.....	1
1.1 Motivation.....	1
1.2 Thesis outline	5
II SrTiO₃ BASED TWO-DIMENSIONAL ELECTRON GAS.....	6
2.1 Strontium titanate (SrTiO ₃)	6
2.1.1 Crystal structure.....	7
2.1.2 Electronic structure	8
2.2 Two-dimensional electron gas (2DEG)	9
2.3 Two-dimensional electron gas in SrTiO ₃	10
2.4 Theoretical background of 2DEG in SrTiO ₃	24

CONTENTS (Continued)

	Page
III PHOTOEMISSION SPECTROSCOPY	27
3.1 Photoelectric effect.....	27
3.2 Photoemission spectroscopy	29
3.3 Angle-resolved photoemission spectroscopy.....	29
3.4 Photoemission process.....	31
3.4.1 The three steps model.....	31
3.4.2 The one step model	32
3.5 Photoemission theory	33
3.6 ARPES system and experiment detail.....	37
3.7 Sample preparation for ARPES measurement.....	40
IV RESULTS AND DISCUSSIONS	42
4.1 Experimental Results of the electronics structure.....	42
4.1.1 Valence band spectrum	42
4.1.2 Band dispersion	43
4.1.3 Fermi surface map.....	45
4.1.4 Effective mass.....	46
4.1.5 Density of carrier	47
4.2 The calculation of band dispersion.....	48

LIST OF TABLES

Table	Page
4.1 The comparison of our observation between SrTiO ₃ (110) and other orientations	48



LIST OF FIGURES

Figure	Page
2.1 The crystal structure of strontium titanate in real (R)-space (left) (Cowley, 1964) and the brillouin zone for the simple cubic lattice (Mattheiss, 1972b).....	7
2.2 (a) Atom positions in cubic SrTiO ₃ (b) Arrows indicate the displacement of the oxygen atoms in the tetragonal state. (c) The projection of one layer of titanium and oxygen atoms on a (001) plane (Mattheiss, 1972b)....	8
2.3 Electronic band structure (left) and density of states (DOS) (right) of SrTiO ₃ in the cubic perovskite structure (Shein and Ivanovskii, 2007).....	9
2.4 The structure of LAO/STO interfaces of (a) n-type (conducting) and (b) p-type interfaces (insulating) (Ohtomo and Hwang, 2004).....	11
2.5 The resistance (a) and mobility (b) at the p-type (blue lines) and n-type interfaces (red lines) as a function of the thickness of LAO at room temperature and the O ₂ pressure 3×10^{-5} mbar (Huijben et al., 2006).....	12

LIST OF FIGURES (Continued)

Figure	Page
<p>2.6 Influence of LaAlO₃ thickness on the electronic properties of the LaAlO₃/SrTiO₃ interfaces. (A) Sheet conductance and (B) carrier density of the heterostructures plotted as a function of the number of their LaAlO₃ unit cells. The data had shown in blue and red are those of samples grown at 770°C and 815°C, respectively. The data were taken at 300 K. The numbers next to the data points indicate the number of samples with values that are indistinguishable in this plot (Thiel et al., 2006).....</p>	13
<p>2.7 (a) T-dependence of the resistance of samples grown at P_{O2} = 10⁻⁶-10⁻³ mbar; grey symbols correspond to the sample grown at 10⁻⁶ mbar after removing the LAO film by mechanical polishing and (b) dependence of the mobility at 4K on the deposition pressure (Herranz et al., 2007).....</p>	14
<p>2.8 The resistance as a function of temperature with different pressure of LAO/STO interface (Brinkman et al., 2007).....</p>	15

LIST OF FIGURES (Continued)

Figure	Page
<p>2.9 Band diagram of the metallic LaAlO₃/TiO₂-SrTiO₃ interface. The band gaps of SrTiO₃ and LaAlO₃ are 3.2 eV and 5.6 eV, respectively. The valence band maximum (VBM) of SrTiO₃ is located at 2.9–3.0 eV. As a consequence of downward band bending, a notched structure is formed in the SrTiO₃ layer in the interfacial region. A band diagram of the metallic LAO/STO heterointerface, as deduced from the PES experiments (Yoshimatsu et al., 2008).....</p>	16
<p>2.10 (a) The resistance at the interface of LAO/STO and (b) the quantum phase transition (QPT) between 2D-superconducting state and an insulating ground state (Caviglia et al., 2008).....</p>	17
<p>2.11 Temperature dependence of the sheet carrier density (a) and (b) mobility of (110) -oriented LAO/STO interface with different LAO layer thickness. And (c) the dependence of the mobility at T = 5 K as a function of carrier density at each value of LAO thickness (Herranz et al., 2012).....</p>	18
<p>2.12 The valance band (VB) spectrum of SrTiO₃. The inset shows the evolution of the in-gap state with increasing exposure to UV light (Meevasana et al., 2011).....</p>	20

LIST OF FIGURES (Continued)

Figure	Page
2.13 (a)-(e) are the energy dispersive curve and (f) is charge density with irradiation dose of SrTiO ₃ at the temperature 20 K (Meevasana et al., 2011).....	20
2.14 The 2DEG states of SrTiO ₃ after exposure synchrotron (UV) light. (a) ARPES data of SrTiO ₃ at T = 20 K, with corresponding momentum distribution curves in (b). (b) the parabolic fits to the data points from the ARPES data. (c) Fermi surface map from the ARPES data. (d) shows the schematic Fermi surface and band dispersions obtained from the measured electronic structure (Meevasana et al., 2011).....	21
2.15 The subbands for the 2DEG at the surface of SrTiO ₃ . Side-by-side representation of the linear-vertical polarization (LV) and the linear-horizontal polarization (LH) spectra around Γ_{102} for the undoped sample. (Santander-Syro et al., 2011).....	22

LIST OF FIGURES (Continued)

Figure	Page
2.16 Conduction band of SrO-terminated SrTiO ₃ (001) surface (a) with no doping, with the concentration of surface La-doping of (b) $0.41 \times 10^{14} \text{cm}^{-2}$ and (c) $1.65 \times 10^{14} \text{cm}^{-2}$. Red solid lines denote the Fermi energy. (d)-(f) Schematic the Fermi surface for the SrO-terminated surface with three concentrations of surface La-doping, respectively (Li and Yu, 2013).....	23
2.17 Schematic energy diagrams of the crystal field splitting and 3 <i>d</i> orbital degeneracy. Two of the 3 <i>d</i> orbitals on the Ti-ion point directly toward the six O ions. The other three orbitals (3 <i>d</i> _{xy} , 3 <i>d</i> _{xz} , and 3 <i>d</i> _{yz}) lie between the O-ions).....	25
2.18 Schematic energy diagrams of the crystal field splitting and 3 <i>d</i> orbital degeneracy, showing the orbital reconstruction at the interface and local bonding change. O _h denotes the octahedral environment (Salluzzo et al., 2009).....	26

LIST OF FIGURES (Continued)

Figure	Page
3.1 Illustration of the photoemission process where Fermi level (E_F), vacuum level (E_{vac}), work function of sample (Φ), kinetic energy of photoelectron (E_{kin}), binding energy (E_B) in material are represented in this model (Comin and Damascelli, 2013).....	28
3.2 Schematic illustration of ARPES system, consisting of incident photon light, sample and analyzer (Zhang, 2013).....	30
3.3 Three-step and one-step model description of the possible photoemission process (Hüfner, 1995).....	33
3.4 The diagram of beamline equipment consisted of a plane grating monochromator, optical slits, and electron analyzer (Damascelli, 2004).....	38
3.5 The high energy resolution ARPES at beamline 10.0.1 of the Advanced Light Source, USA.....	39
3.6 Crystal structure of $SrTiO_3(110)$, the 2D unit cell in real-space and reciprocal-space of $(SrTiO)^{4+}$ surface.....	41
3.7 Laue pattern of STO(110) reflecting to the perfect rectangle shape with sharp spots	41

LIST OF FIGURES (Continued)

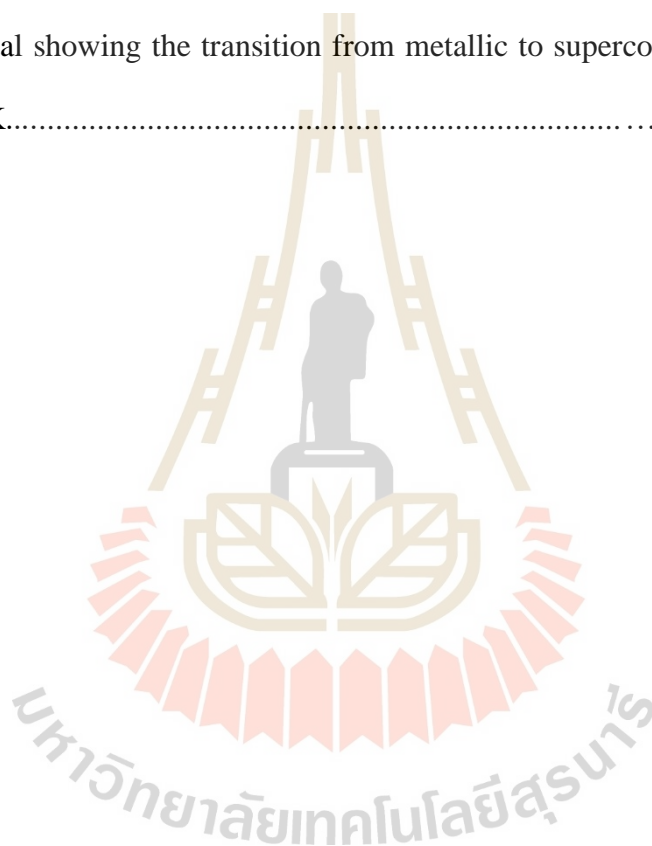
Figure	Page
4.1 the valence band spectrum of oxygen $2p$ (O_{2p}) state between 3-10 eV, the in-gap state, and 2DEG state (insect) after exposing UV light.....	43
4.2 (a) and (b) show the band dispersion of La doped (110)-oriented $SrTiO_3$ surface which measure in the direction of k_M at the Γ_{10} while (c) and (d) were measure in the direction of k_Z at the Γ_{11} for p -pol and s -pol light.....	44
4.3 Fermi surface maps along the k_m -direction with p -polarized light (a) and s -polarized light (b) at the Γ_{10} -point, and along k_z -direction with p -polarized light at the Γ_{11} -point (c), momentum distribution curves with corresponding to (a-c) in figure 4.2, respectively, and (d) the schematic Fermi surface map of all (a-c).....	46
4.4 The band structure of $SrTiO_3$ (110) calculate by using a self-consistent tight-binding super cell compare to the experiment in the direction of k_M and k_Z (the white lines are ARPES data).....	49
4.5 The thermoelectric figure of merit (ZT) of $SrTiO_3$ 2DEG and bulk as a function of density of state (n_s) (Ohta et al., 2007).....	51
4.6 STO supercell containing oxygen vacancy (Mitra et al., 2012).....	52

LIST OF FIGURES (Continued)

Figure	Page
4.7 Structure of 2x2x6 SrTiO ₃ slabs with oxygen vacancy in (a) the SrO and (b) TiO ₂ Surface layer, and (c) the layer-decomposed electron filling of the gap states close to the Fermi level as a function of depth. The layers are numbered from the bottom of the slab and the oxygen vacancy has been introduced on the top layer (Shen et al., 2012).....	53
B.1 The cryostat system including an expander, a compressor and a temperature controller.....	75
B.2 Real setup of our cryostat system consisting of; cryostat chamber, temperature controller, turbo pump, and water chiller....	75
B.3 Simple diagram of the cryostat system.....	76
B.4 Prototype of LabVIEW front panel using to measure resistance in our cryostat setup.....	77
B.5 Block diagram for controlling the operation of system.....	77
B.6 Sample preparation, sample were mounted with the sample holder by spotted welding and wired with silver wire. The silver wire will be connected to the electrical port to make an electrode for 4-point probe measurement....	78

LIST OF FIGURES (Continued)

Figure	Page
B.7 Diagram of two- and four-point probe method.....	79
B.8 Temperature dependence of the measured voltage (constant current) of Nb metal showing the transition from metallic to superconducting phase at 9.4 K.....	80



LIST OF ABBREVIATIONS

1D, 2D	=	One-dimension, Two-dimension
2DEG	=	Two-dimensional electron gas
ARPES	=	Angle-resolved photoemission
TMO	=	Transition metal oxide
STO	=	Strontium titanate (SrTiO_3)
LAO	=	Lanthanum aluminium oxide (LaAlO_3)
QPT	=	Quantum phase transition
DFT	=	Density functional theory
2DEL	=	Two-dimensional electron liquid
FSM	=	Fermi surface map
CBM	=	Conduction band minimum
VBM	=	Valence band maximum
LEED	=	Low energy electron diffraction
UV	=	Ultraviolet
CFT	=	Crystal field theory
PES	=	Photoemission spectroscopy
VUV	=	Vacuum ultraviolet
UPS	=	Ultraviolet photoemission spectroscopy
OV	=	Oxygen vacancy
MDC	=	Momentum dispersion curve

LIST OF ABBREVIATIONS (Continued)

EDC	=	Energy dispersion curve
FWHM	=	Full width at half maximum
PID	=	Proportional integral derivative
FPP	=	Four-point probes



CHAPTER I

INTRODUCTION

1.1 Motivation

The formation of 2DEG at the interfaces or surfaces of transition metal oxides (TMOs), in particular on strontium titanate (SrTiO_3), is a field of active research (Zubko et al., 2011; Hwang et al., 2012; Gabay et al., 2013; Stemmer and Allen, 2014). These interfacing systems exhibit a variety of novel electronic phases e.g. superconductivity (Reyren et al., 2007; Dikin et al., 2011), large magnetoresistance (Brinkman et al., 2007), large capacitance (Skinner and Shklovskii, 2010; Li et al., 2011), thermoelectric (Ohta, 2007; Ohta et al., 2012) and ferromagnetism (Bert et al., 2011; Dikin et al., 2011; Li et al., 2011) which are crucial for opening the new route for developing the functionalities of these materials to future applications in nano-scale and field-effect devices (Cen et al., 2009; Hosoda et al., 2013).

The first observation of 2DEG at the interface was found at the interface between LaAlO_3 and $\text{SrTiO}_3(001)$ system. Both materials are wide-band gap insulators but a conducting state can be formed at their interface with high carrier mobility exceeding to $10^4 \text{ cm}^2\text{V}^{-1}\text{s}^{-1}$ at low-temperature (Ohtomo and Hwang, 2004). However, it depends on the precise atomic stacking, n-type interface is conducting while p-type interface is insulating, the thickness of LaAlO_3 layer (thick was better) and the O_2 pressure during growing the LaAlO_3 on SrTiO_3 substrate (should be low-pressure, $P < 10^{-6}$ mbar).

These results indicated that the mechanisms of 2DEG emerging at the interface may be possibly cause by two reasons; i) polar discontinuity and ii) oxygen vacancy. To study this issue, there were many observations about the interface of LAO/STO and then found that 2DEG can be found both at the p and n-type interface. Furthermore, the insulating state became to the conducting state when the thickness of LAO was more than the critical thickness (D_c). The conductivity was reduced when the thickness of LaAlO_3 below 6 unit cells, $D_c = 6$ uc or $< 23 \text{ \AA}$ (Huijben et al., 2006).

Most of experiments seemed to verify the mechanism of polar discontinuity because the polar discontinuity was relative to the thickness of LaAlO_3 , high polar discontinuity if the thickness was large which respond to high conductivity. Although there were the experimental data that strongly support an interpretation of these properties based on the creation of oxygen vacancies in the SrTiO_3 substrates during the growth of the LaAlO_3 layer (Herranz et al., 2007), the samples grown with low-oxygen pressure have more oxygen vacancies and with consequently more conducting. The conductivity reduced if the samples were grown in high pressure O_2 . However, the reason is still not clear (Herranz et al., 2007; Kalabukhov et al., 2007; Siemons et al., 2007; Liu et al., 2013).

Amid suspicions, the field effect was under investigation. By applying the voltage into the $\text{LaAlO}_3/\text{SrTiO}_3(001)$ interface, an insulating state at the interface can be transformed to be a metallic state when the thickness of LaAlO_3 when the thickness more than 4 unit cells, $d_c = 4$ uc. Sheet conductance = $4 \times 10^{-3} \text{ ohm}^{-1}$ (at 4.2 K) and $2 \times 10^{-5} \text{ ohm}^{-1}$ (at 300 K) and all samples with $d_c < 3$ uc, insulating, Sheet conductance $< 2 \times 10^{-10} \text{ ohm}^{-1}$ at all temperature. According to Hall measurements done on the conducting samples, their carriers are negatively charged with mobility of

1200 cm² V⁻¹ s⁻¹ and 6 cm² V⁻¹ s⁻¹ at 4.2 K and 300 K, respectively, and densities reached to 10¹³ cm⁻² (Thiel et al., 2006).

It was also found that a superconducting state can be tuned by inducing the external electric-field under the growth condition at high pressure of O₂ and depend on the thickness of LaAlO₃. When $d_c = 8$ uc, the critical temperature (Herranz et al., 2013) was about 200 mK which provided a strict upper limit to the thickness of the superconducting layer of $\cong 10$ nanometers, ($d_{SC} = 10$ nm) Furthermore, the quantum phase transition (QPT) between 2D-superconducting state and an insulating ground state was reported that it can be controlled by switching on/off the voltage to tune the carrier density (Caviglia et al., 2008). The coexistence of ferromagnetic and superconductivity also occurred by sourcing a magnetic field (Bert et al., 2011; Dikin et al., 2011; Li et al., 2011). This has never seen in the other superconductors. These observations open the new way to the design of devices and the development of mesoscopic superconducting circuits in oxide electronics.

Nevertheless, there was an observation of 2DEG in the other orientations of LaAlO₃/SrTiO₃ interfaces. Although their interfaces have no polar discontinuity where differs from the (001)-oriented LaAlO₃/SrTiO₃ interface, the high-mobility 2DEG can be created at the (110) and (111) -oriented LaAlO₃/SrTiO₃ interfaces (G. Herranz et al., 2012). Furthermore, the superconductivity can be tuned by orientation. At temperature below 200 mK, the 2D-superconducting thickness of (110)-oriented LaAlO₃/SrTiO₃ interface ($d_{SC} = 24-30$ nm) (Herranz et al., 2013) was significantly larger than that of (001)-oriented LaAlO₃/SrTiO₃ interface ($d_{SC} = 10$ nm) (Reyren et al., 2007). This property differs from the other superconductors; it has never seen the way to tune the electronic structure by changing the crystallographic orientation. In addition, it was also

shown that the unexpected conductivity was strongly anisotropic along the different crystallographic directions with potential for anisotropic superconductivity and magnetism, leading to possible new physics and applications. However, from density functional theory (DFT) calculation, the buckled TiO_2/LaO was considered to be the causes of polar discontinuity of (110)-interfaces (Annadi et al., 2014).

Beyond the realization of 2DEG at interfaces, it was discovered that 2DEG can be simply created at the vacuum-cleaved surface of insulating SrTiO_3 , which was a non-polar surface of two types of SrO and TiO_2 terminating surfaces (Meevasana et al., 2011; Santander-Syro et al., 2011). By shining the ultraviolet light, 2DEG of La-doped $\text{SrTiO}_3(100)$ can be induced with an electron density as large as $8 \times 10^{13} \text{ cm}^{-2}$ and an effect mass (m^*) of $(0.5-0.6)m_e$, (m_e is free electron mass), which can be controlled by an irradiation dose (Meevasana et al., 2011). However, it was described by the two-dimensional electron liquid (2DEL) because spectral features enhanced by strong electron correlations.

At that moment, it was also found that the 2DEG of undoped $\text{SrTiO}_3(001)$ surface was induced by oxygen vacancy consists of multi-band of heavy and light electrons with effective mass of $(10-20)m_e$ and $0.7 m_e$, respectively which contributed to the electron density of about $2 \times 10^{14} \text{ cm}^{-2}$ (Santander-Syro et al., 2011). Moreover, 2DEG at $\text{SrTiO}_3(100)$ surface was also reported that it can be induced and tuned by changing the doping La concentration at the SrO-terminated surface, with has an effective mass as small as $0.44 m_e$ (Li and Yu, 2013). Recently, it has reported that the co-operative effect of orbital ordering and electron-phonon coupling dominate the spin splitting which is a cause of the quasi-particle dynamics of the d-electron subband ladder of this complex-oxide 2DEG and can be directly observed by angle-resolved photoemission

(King et al., 2014). Moreover, it has also shown that 2DEG can be induced at a polar surface of SrTiO₃ in (110)-orientation which was dominated by oxygen vacancy using synchrotron radiation. The band is quantized into two bands of lightly and semi-heavy band and shows an anisotropic conducting (Wang et al., 2014). These imply that the interface and the polar field are no longer necessary for the creation of 2DEG, which have opening an exciting perspective to create novel 2DEGs at the surface of correlated oxides of (110)-oriented SrTiO₃.

1.2 Thesis outline

In this thesis, we investigate the electronic structure of two-dimensional (2D) electron gas of a polar surface of SrTiO₃(110) using angular resolved photoemission spectroscopy (ARPES), which is the sensitive technique for surface science. The thesis consists of five main chapters as followed. Chapter I introduces the motivation about why we are interested in the electronic structure of two-dimensional electron gas of SrTiO₃(110) surfaces. Chapter II reviews the background of strontium titanate (SrTiO₃), two-dimensional electron gas (2DEG) and both of theoretical and experimental background of two-dimensional electron gas (2DEG) in SrTiO₃. Chapter III described the technical background of photoemission spectroscopy including photoelectric effect, photoemission spectroscopy, photoemission process, angle resolve photoemission spectroscopy (ARPES), and sample preparation for ARPES measurement. Chapter IV shows the experimental and calculating results of electronics properties including the valence band and dispersion spectra, the Fermi surface map, the effective mass, the density of carriers, and discusses the results compared to the calculation. Finally, the overall conclusion of this thesis is given in chapter V.

CHAPTER II

SrTiO₃ BASED TWO-DIMENSIONAL ELECTRON GAS

2.1 Strontium titanate (SrTiO₃)

Strontium titanate (SrTiO₃ or STO) is a one type of transition metal oxides which may be used as a platform of multifunctional oxide devices. It has been studied extensively for over half a century. Because of its interesting properties and the simple of crystalline structure, it is an ideal perovskite material and its interesting properties could be investigated by an experimental observation. Indeed, SrTiO₃ has a similar structure and lattice constant to many other important oxides allowing for their epitaxial growth which plays an important role as a standard substrate. For example, it is possible to grow high-T_c superconductors (Chaudhari et al., 1987) and it can be grown on Si (Zollner et al., 2000) which provides a route to integrate oxide-based devices into microelectronic industry. In addition, it also exhibits the variety phenomena such as colossal magnetoresistance (Brinkman et al., 2007), large capacitance (Skinner and Shklovskii, 2010; Li et al., 2011), giant dielectric (Takesada et al., 2003), ferroelectrics (Itoh et al., 1999; Lee et al., 2010), thermoelectric effect (Ohta et al., 2007; Ohta, 2013), superconductivity (Reyren et al., 2007), and ferromagnetism (Bert et al., 2011; Dikin et al., 2011; Chen and Balents, 2013), which are useful for application of nanoelectronics and spintronic devices.

2.1.1 Crystal structure

Strontium titanate (STO) is a perovskite structure which has a chemical formula ABO_3 in space group $Pm\bar{3}m$, where the A is Sr (an alkaline metal) whereas the B is Ti (a first-row transition metal) and O is oxygen. The bulk structure of STO is a cubic-phase at the room temperature which has a lattice constant 3.905 \AA (Cowley, 1964) The Sr atoms are located at the corner $(0, 0, 0)$ of unit cell and the Ti is at the center of the cube $(\frac{1}{2}, \frac{1}{2}, \frac{1}{2})$, surrounded by six oxygen that occupy the middle of the faces, in a regular octahedral configuration of TiO_6 (O_h Symmetry) as shown in figure 2.1.

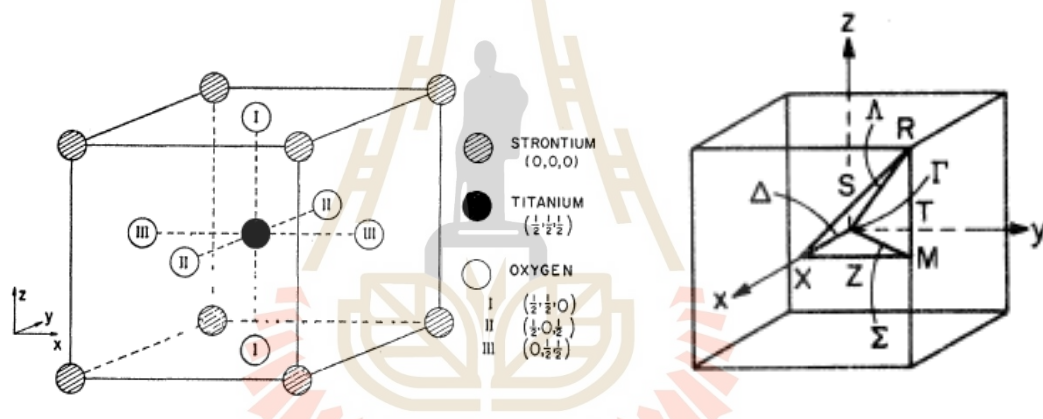


Figure 2.1 The crystal structure of strontium titanate in real (R)-space (left) (Cowley, 1964) and the Brillouin zone (right) for the simple cubic lattice (Mattheiss, 1972b).

The TiO_6 octahedral is perfect with 90° angles and six equal Ti-O bonds at 1.952 \AA . Each Sr atom is surrounded by twelve equidistant oxygen atoms at 2.76 \AA (Orhan et al., 2004). At low-temperature, the cubic phase transforms to tetragonal phase at the transition temperature $105\text{-}110 \text{ K}$ (Fleury et al., 1968; Mattheiss, 1972a). In this transition, a structural transformation of neighboring octahedral TiO_6 complexes is

rotated rigidly in opposite directions about the c axis through small angles $\pm\phi$ (see figure 2.2).

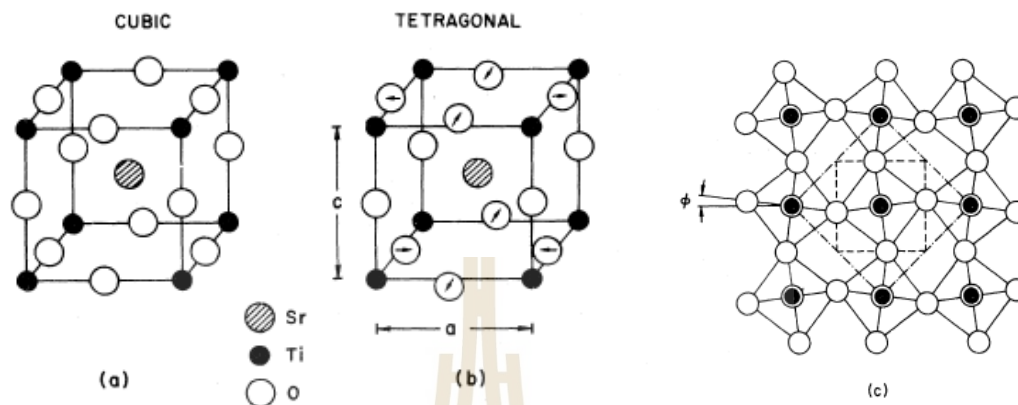


Figure 2.2 (a) Atom positions in cubic SrTiO₃ (b) Arrows indicate the displacement of the oxygen atoms in the tetragonal state. (c) The projection of one layer of titanium and oxygen atoms on a (001) plane (Mattheiss, 1972b).

2.1.2 Electronic structure of bulk SrTiO₃

SrTiO₃ is an insulator with an optical band gap of 3.22 eV (Noland, 1954; Kahn and Leyendecker, 1964; Cardona, 1965; Van Benthem et al., 2001). The conduction band minimum (CBM) is derived from Ti3*d* states and the valence band maximum (VBM) is dominated O2*p* states (Mattheiss, 1972b). There were many reports on the study of electronic structure in SrTiO₃. For examples, the calculation of band structure and the density of states shown in figure 2.3, which found the conduction band minimum at the Γ -point and the valence band maximum at the R-point with the indirect gap of 1.81 eV (Shein and Ivanovskii, 2007).

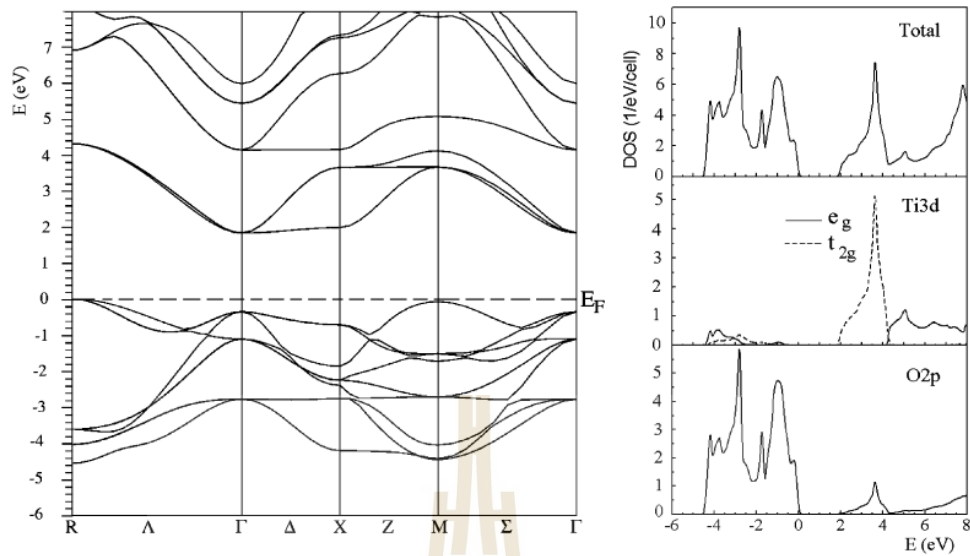


Figure 2.3 Electronic band structure (left) and density of states (DOS) (right) of SrTiO₃ in the cubic perovskite structure (Shein and Ivanovskii, 2007).

2.2 Two-dimensional electron gas (2DEG)

The two-dimensional electron gas (2DEG) is a gas of electrons free to move in two dimensions, but tightly confined in the perpendicular direction. This tight confinement leads to quantized energy level for motion in the third direction, which can be ignored for most problems.

To understand the figure of 2DEG state, we can consider the system of electrons in the box of width L . When the spatial expansion of a material becomes smaller than the wavelength of the conduction electrons, electrons become confined and their energy E as well as their momentum k becomes quantized. This leads to the electronic properties dominated by quantum size. The potential describing the box is given by

$$V(x) = \begin{cases} 0, & \text{for } 0 < x < L \\ \infty, & \text{else} \end{cases} \quad (2.1)$$

Solving the Schrödinger equation gives the following energy eigenvalues

$$E(\vec{k}) = \frac{\hbar^2 k^2}{2m} \quad (2.2)$$

Where m is the mass of particle, $k = n\pi/L$, and $n \in \mathbf{N}$. Electrons can be confined in one spatial direction in a quantum well, in two spatial directions in a quantum wire, and in all three spatial directions in a quantum dot. In the following we will focus on the two-dimensional electron gas (2DEG) where the electrons are confined along one direction but are allowed to move freely in the plane. Such 2DEGs are of particular interest because they show the (fractional) quantum Hall effect. 2DEGs located on the surface of a substrate are of particular importance in the field of surface science because they can be investigated by surface sensitive techniques for example low energy electron diffraction (LEED), scanning tunneling microscopy (STM), and angular resolved photoemission spectroscopy (ARPES).

2.3 Two-dimensional electron gas in SrTiO₃

Since the discovery of the 2DEG at the SrTiO₃/LaTiO₃ interface in 2004 by Ohtomo and Hwang (Ohtomo and Hwang, 2004). Many experimental data have been reported for this system. Growth conditions, such as oxygen partial pressure and annealing temperature, have been identified as the major factor that controls the

electronic properties of the 2DEG. Moreover, it was also found that 2DEG could be emerged at SrTiO₃ surface.

In 2004, Ohtomo and Hwang (Ohtomo and Hwang, 2004) found that at the interface of LaAlO₃ and SrTiO₃(001) system exhibited 2DEG with high carrier mobility exceeding to $10^4 \text{ cm}^2\text{V}^{-1}\text{s}^{-1}$ at low-temperature as shown in the figure 2.4. Both materials of LaAlO₃ and SrTiO₃ are wide-band gap insulators (LAO = 5.6 eV, STO = 3.2 eV), and they are reasonably well lattice matched to one another (LAO = 3.789 Å, STO = 3.905 Å). However, it depends on the precise atomic stacking, n-type interface is conducting while p-type interface is insulating, the thickness of LaAlO₃ layer (thick was better) and the O₂ pressure during growing the LaAlO₃ on SrTiO₃ substrate (should be low-pressure, $P < 10^{-6}$ mbar). This experiment explained that 2DEG was induced at the interface because of the polar discontinuity which leads to the charge transfer from the LaO layer into the TiO₂ layer.

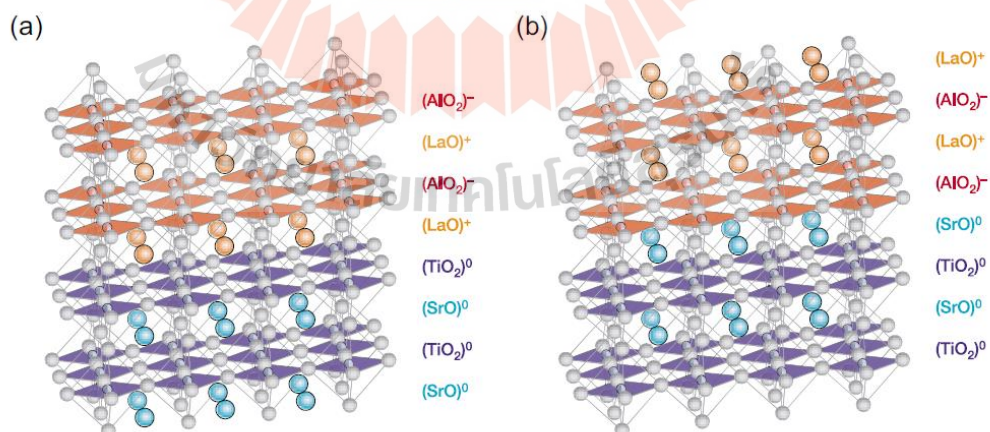


Figure 2.4 The structure of LAO/STO interfaces of (a) n-type (conducting) and (b) p-type interfaces (insulating) (Ohtomo and Hwang, 2004).

Later, Huijben et al. (Huijben et al., 2006) grew LaAlO_3 film on TiO_2 -terminated SrTiO_3 surface creating TiO_2/LaO (n-type) interface and then capping layer of SrTiO_3 on LaAlO_3 creating AlO_2/SrO (p-type) interface. The 2DEG can be formed both of them and the insulating became to the conducting state when the thickness of LAO was more than the critical thickness (D_c) as illustrated in figure 2.5. The conductivity was reduced when the thickness of LAO below 6 unit cells ($D_c = 6$ uc or 23 \AA). This observation indicates that the oxygen vacancy is the origin of 2DEG at the interfaces.

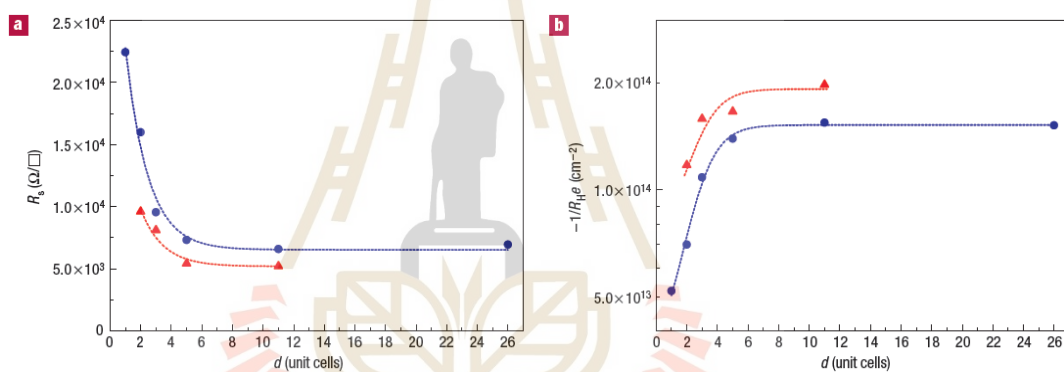


Figure 2.5 The resistance (a) and mobility (b) at the p-type (blue lines) and n-type interfaces (red lines) as a function of the thickness of LAO at room temperature and the O_2 pressure of 3×10^{-5} mbar (Huijben et al., 2006).

After that, there are many experiments about the interface of LAO/STO to observe the mechanisms of 2DEG emerging at the interface, which may be possibly caused by two reasons; i) polar discontinuity and ii) oxygen vacancy.

To study the polar discontinuity at the interface, there was the study which increased the polar discontinuity by applying the voltage into the $\text{LaAlO}_3/\text{SrTiO}_3(001)$

interface. Thiel et al. (Thiel et al., 2006) observed that for samples grown under relatively high oxygen partial pressure the n-type LAO/STO interface is not conducting unless the thickness of LaAlO₃ film exceeds a critical value of four unit cells. An insulating state at the interface can be transformed to be a metallic state when the thickness of LaAlO₃ more than 4 unit cells ($d_c = 4uc$) with the densities reached to 10^{13} cm⁻². Sheet conductance = 4×10^{-3} ohm⁻¹ (at 4.2 K) and 2×10^{-5} ohm⁻¹ (at 300 K), respectively.

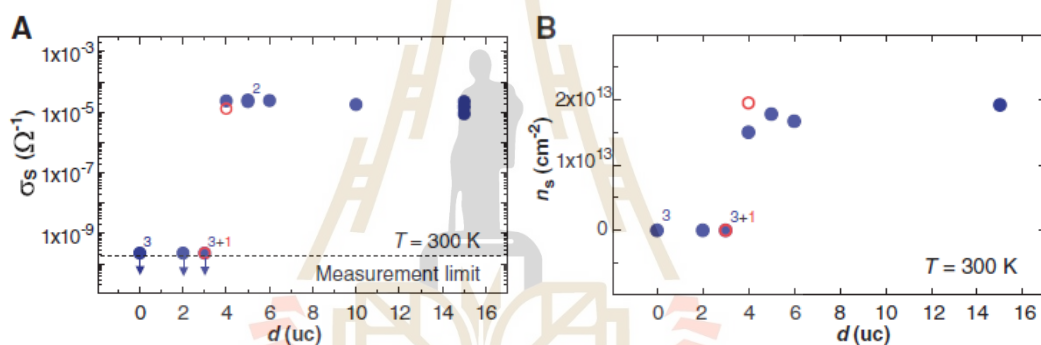


Figure 2.6 Influence of LaAlO₃ thickness on the electronic properties of the LaAlO₃/SrTiO₃ interfaces. (A) Sheet conductance and (B) carrier density of the heterostructures plotted as a function of the number of their LaAlO₃ unit cells. The data shown in blue and red are those of samples grown at 770°C and 815°C, respectively. The data were taken at 300 K. The numbers next to the data points indicate the number of samples with values that are indistinguishable in this plot (Thiel et al., 2006).

Most of experiments seemed to verify the mechanism of polar discontinuity because the polar discontinuity was relative to the thickness of LaAlO₃, high polar

discontinuity if the thickness was large, corresponds to high conductivity. Although the experimental data strongly support an interpretation of these properties based on the creation of oxygen vacancies in the SrTiO₃ substrates during the growth of the LaAlO₃ layer (Brinkman et al., 2007; Herranz et al., 2007; Kalabukhov et al., 2007; Siemons et al., 2007; Liu et al., 2013), the samples grown with low-oxygen pressure have more oxygen vacancies and with consequently more conducting; the conductivity reduced if the samples were grown in high pressure O₂.

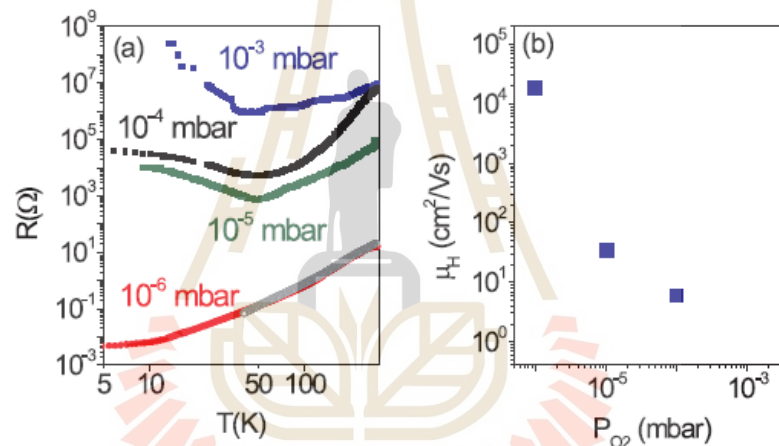


Figure 2.7 (a) T-dependence of the resistance of samples grown at $P_{O_2} = 10^{-6}$ - 10^{-3} mbar; grey symbols correspond to the sample grown at 10^{-6} mbar after removing the LAO film by mechanical polishing and (b) dependence of the mobility at 4K on the deposition pressure (Herranz et al., 2007).

Herranz et al. (Herranz et al., 2007) observed the resistance and mobility of the LAO/STO interface and the experimental data strongly support an interpretation of these properties based on the creation of oxygen vacancies in the SrTiO₃ substrates during the growth of the LaAlO₃ layer. At higher P_{O_2} the conduction is dramatically

suppressed and non-metallic behavior appears as show in figure 2.7. Similar to the observation of Brinkman (Brinkman et al., 2007), it was also found that the LAO/STO interface could be conductive at low deposition oxygen pressures ($P_{O_2} < 10^{-6}$ mbar) as shown in figure 2.8.

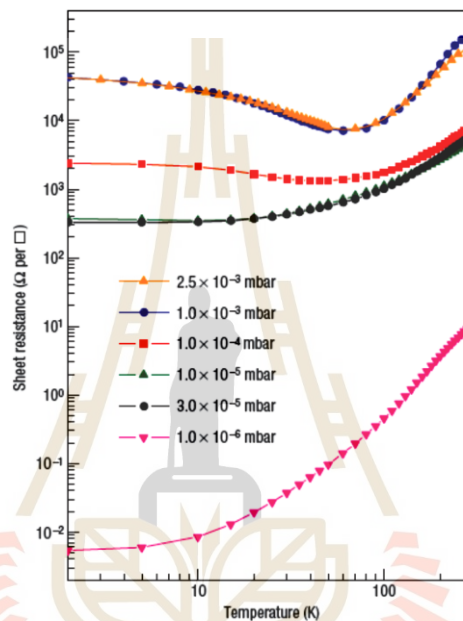


Figure 2.8 The resistance as a function of temperature with different pressure of LAO/STO interface (Brinkman et al., 2007).

Moreover, Yoshimatsu et al. (Yoshimatsu et al., 2008) investigated that the interfacial electronic structures are responsible for the metallic states in the LAO/STO interface using PES technique. And then they explained that the notched structure was formed in the STO layers in the interfacial region, depending on the terminating layer of the interface. These results indicate that the metallic conductivity originate not from

the charge transfer through the interface but from the accumulation of carriers on the notched structure at the interface as illustrated in figure 2.9.

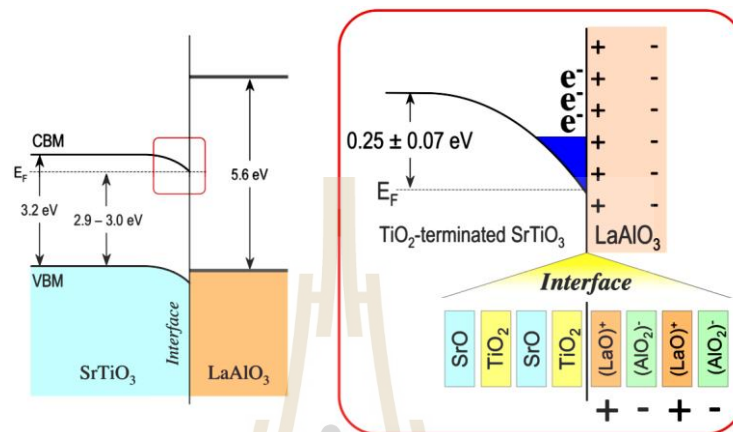


Figure 2.9 Band diagram of the metallic $\text{LaAlO}_3/\text{TiO}_2\text{-SrTiO}_3$ interface. The band gaps of SrTiO_3 and LaAlO_3 are 3.2 eV and 5.6 eV, respectively. The valence band maximum (VBM) of SrTiO_3 is located at 2.9–3.0 eV. As a consequence of downward band bending, a notched structure is formed in the SrTiO_3 layer in the interfacial region. A band diagram of the metallic LAO/STO heterointerface, as deduced from the PES experiments (Yoshimatsu et al., 2008).

In addition, the quantum phase transition (QPT) between 2D-superconducting state and an insulating ground state was reported that it can be controlled by switching on/off the voltage to tune the carrier density (Caviglia et al., 2008). The coexistence of ferromagnetic and superconductivity was replaced by sourcing a magnetic field (Bert et al., 2011; Dikin et al., 2011; Li et al., 2011) which has never seen in the other

superconductors. These observations open the new way to design the devices and the development of mesoscopic superconducting circuits in oxide electronics.

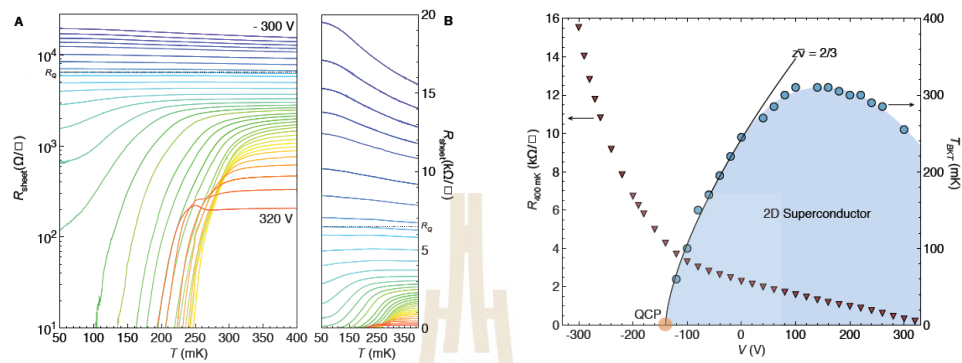


Figure 2.10 (A) The resistance at the interface of LAO/STO and (B) the quantum phase transition (QPT) between 2D-superconducting state and an insulating ground state (Cavaglia et al., 2008).

Nevertheless, there was an observation of 2DEG in the other orientations of $\text{LaAlO}_3/\text{SrTiO}_3$ interfaces. Herranz et al. (Herranz et al., 2012) found that the high-mobility 2DEG can be created at the (110) and (111)-oriented $\text{LaAlO}_3/\text{SrTiO}_3$ interfaces. For (110)-oriented $\text{LaAlO}_3/\text{SrTiO}_3$ interfaces, the sheet carrier density and electronic mobility increased up to $1 \times 10^{14} \text{ cm}^{-2}$ and $2500 \text{ cm}^2/\text{Vs}$ respectively, (see figure 2.11) which was very similar to those found in (001)-interfaces but their interfaces have no polar discontinuity as (001)-interfaces.

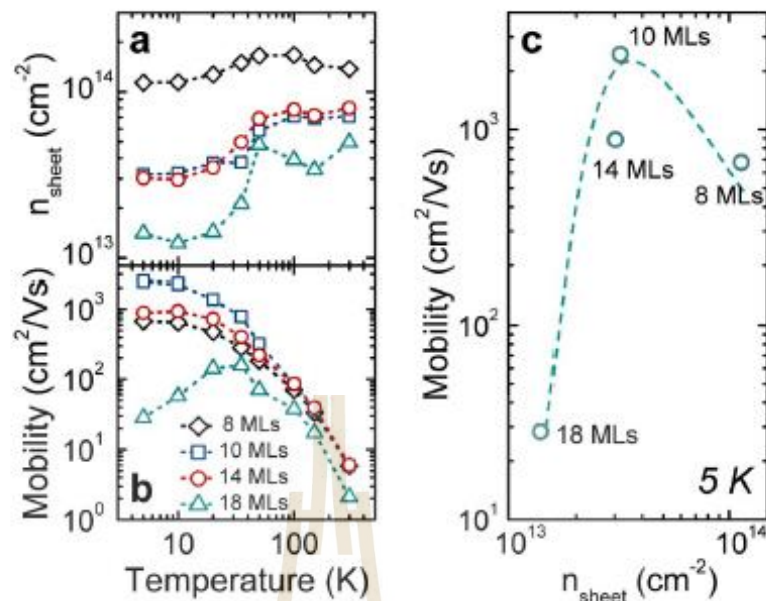


Figure 2.11 Temperature dependence of the sheet carrier density (a) and (b) mobility of (110)-oriented LAO/STO interface with different LAO layer thickness. And (c) the dependence of the mobility at $T = 5 \text{ K}$ as a function of carrier density at each value of LAO thickness (Herranz et al., 2012).

Furthermore, the superconductivity can be tuned by orientation. At temperature below 200 mK, the 2D-superconducting thickness of (110)-oriented $\text{LaAlO}_3/\text{SrTiO}_3$ interface ($d_{\text{SC}} = 24\text{-}30 \text{ nm}$) (Herranz et al., 2013) was significantly larger than that of (001)-oriented $\text{LaAlO}_3/\text{SrTiO}_3$ interface ($d_{\text{SC}} = 10 \text{ nm}$) (Reyren et al., 2007). This property differs from the other superconductors as the way to tune the electronic structure by changing the crystallographic orientation is never reported before. In addition, it was shown that the unexpected conductivity was strongly anisotropic along the different crystallographic directions with potential for anisotropic superconductivity and magnetism, leading to possible new physics and applications. However, from

density functional theory (DFT) calculation, the buckled TiO_2/LaO was considered that is a cause of polar discontinuity of (110)-interfaces (Annadi et al., 2014).

Recently, researchers found that 2DEG can also be formed at the vacuum-cleaved surface of insulating SrTiO_3 , (Meevasana et al., 2011; Santander-Syro et al., 2011) rather than forming at the interfaces or applying polar electric field. They suggested that oxygen vacancies at the UV-irradiated surface play an important role to driven this. By using ARPES, they showed that 2DEG and in-gap state could be observed after shining UV light at the cleaved-surface of La-doped $\text{SrTiO}_3(100)$ at temperature around 20 K as shown in the figure 2.12. At $t = 0$, the spectrum shows clear oxygen 2p (O_{2p}) states between $\sim 3-9\text{eV}$, and no significant spectral weight in the band gap ($0-3\text{eV}$). As the exposure time increases, the spectral weight of the O_{2p} state decreases slightly and its leading edge shifts to higher binding energy. This indicates an increase in the valence band maximum to surface Fermi level separation, consistent with a downward band bending and development of a 2DEG at the surface.

This result can be explained that oxygen vacancies were intentionally produced by exposing the surface to an ultraviolet irradiation. The concentration of oxygen vacancies concentration is proportional to the carrier density and thus suggesting that the vacancies are electron donor and it could be changed by changing the dose of irradiation as shown in figure 2.13, and found two band dispersions can with Fermi wave number $k_F = 0.12 \text{ \AA}^{-1}$, and deeper band with $k_F = 0.175 \text{ \AA}^{-1}$, have their band bottoms situated 110 and 216 meV below the Fermi level, respectively as demonstrated in figure 2.14. An electron density as large as $8 \times 10^{13} \text{ cm}^{-2}$ and an effect mass (m^*) of $(0.5-0.6)m_e$, (m_e is free electron mass).

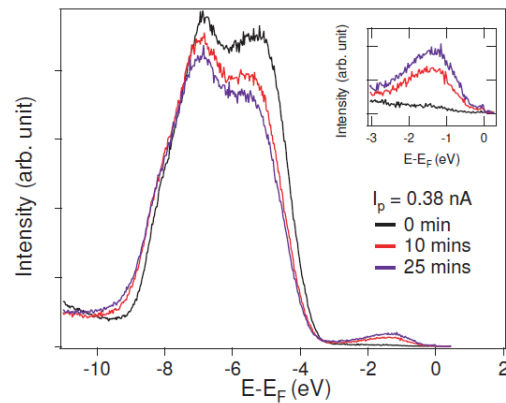


Figure 2.12 The valence band spectrum of SrTiO₃. The inset shows the evolution of the in-gap state with increasing exposure to UV light (Meevasana et al., 2011).

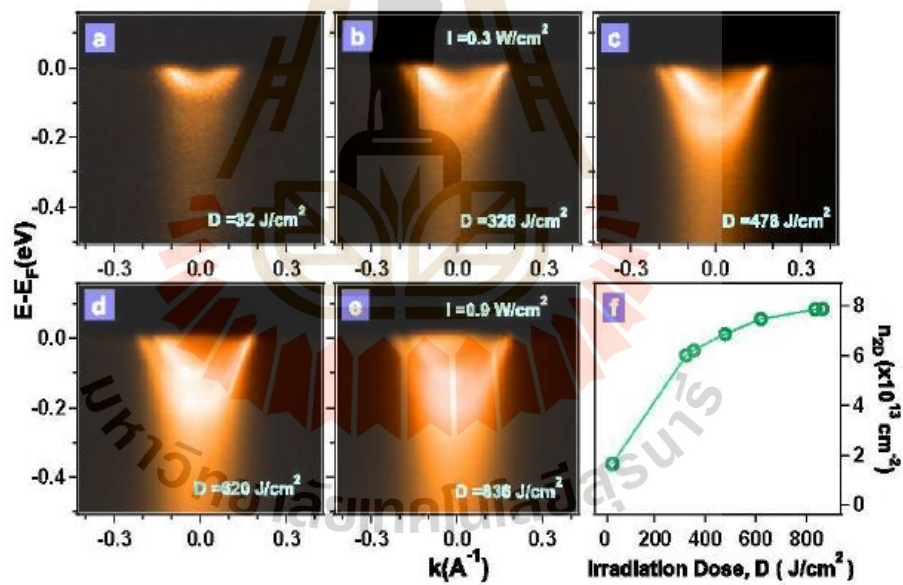


Figure 2.13 (a)-(e) are the energy dispersive curve and (f) is charge density with irradiation dose of SrTiO₃ at the temperature 20 K (Meevasana et al., 2011).

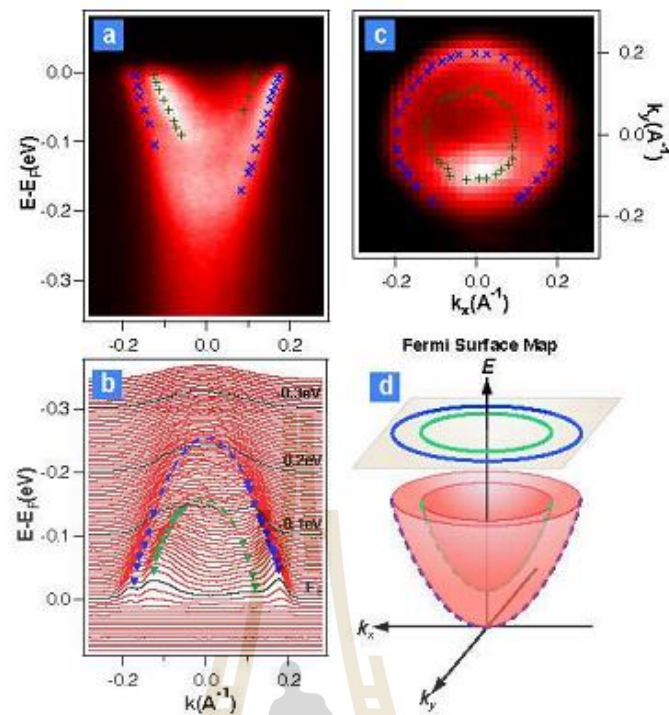


Figure 2.14 The 2DEG states of SrTiO_3 after exposure synchrotron (UV) light. (a) ARPES data of SrTiO_3 at $T = 20$ K, with corresponding momentum distribution curves in (b). (b) the parabolic fits to the data points from the ARPES data. (c) Fermi surface map from the ARPES data. (d) shows the schematic Fermi surface and band dispersions obtained from the measured electronic structure (Meevasana et al., 2011).

Santander et al. (Santander-Syro et al., 2011) found that 2DEGs at pure $\text{SrTiO}_3(001)$ surface consist of multi-band indicated as heavy and light electrons with effective mass of $(10-20)m_e$ and $0.7 m_e$, respectively. Those bands contribute to the electron density reaching $2 \times 10^{14} \text{ cm}^{-2}$. The visibility of each subbands depends on the polarization of light which was used throughout experiment as shown in figure 2.15.

Two subbands have been observed by linear-vertical (LV) light while only one band was detected by linear-horizontal (LH) light.

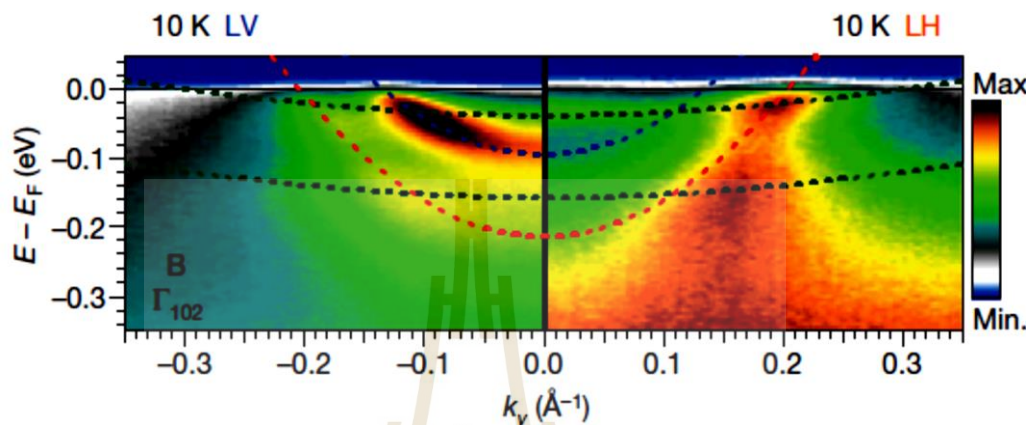


Figure 2.15 Subband structure of 2DEGs at the surface of pure SrTiO₃ around Γ_{102} probed by (left) linear-vertical polarization (LV) and (right) linear-horizontal polarization (LH). (Santander-Syro et al., 2011).

Li and Yu (Li and Yu, 2013) reported that 2DEGs can be formed by introducing La-doping at the SrO-terminated of SrTiO₃(100) surface with has an effective mass as small as 0.44 m_e . The 2DEG density can be tuned by changing the doping concentration. The higher the La-doping concentration, the lower the lower-lying surface state and the higher the 2DEG density as shown in figure 2.16. King's group (King et al., 2014) has reported an interesting phenomena on the surface of STO(100) which is the co-operative effect between orbital ordering and electron-phonon coupling. This behavior results in the emerging of spin splitting of this complex-oxide 2DEG. The quasi-particle dynamics of the d-electron subband ladder of STO(100) have also been observed by ARPES.

Moreover, it has also shown that 2DEG can be induced at a polar surface of SrTiO₃ in (110)-orientation which was dominated by oxygen vacancy using synchrotron radiation. The band is quantized into two bands of lightly and semi-heavy band and shows an anisotropic conducting (Wang et al., 2014). These evidences imply that 2DEG can be created at the surfaces of some oxide materials which is not limited at the interfaces or applying external field.

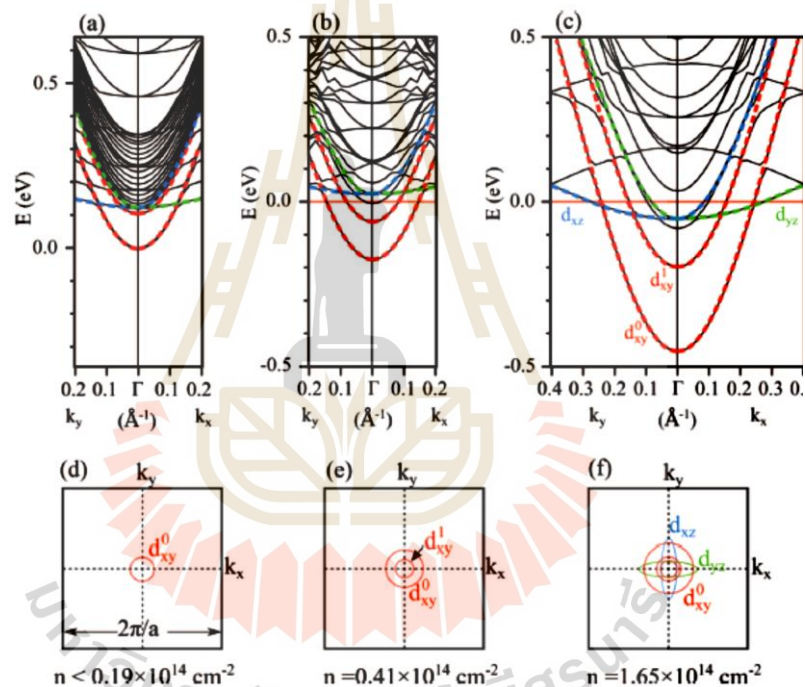


Figure 2.16 Conduction band of SrO-terminated SrTiO₃(001) surface (a) with no doping, with the concentration of surface La-doping of (b) $0.41 \times 10^{14} \text{ cm}^{-2}$ and (c) $1.65 \times 10^{14} \text{ cm}^{-2}$. Red solid lines denote the Fermi energy. (d)-(f) Schematic the Fermi surface for the SrO-terminated surface with three concentrations of surface La-doping, respectively (Li and Yu, 2013).

2.4 Theoretical background of 2DEG in SrTiO₃

Crystal Field Theory (CFT) is a model that describes the effect of the electrical field of neighboring ions on the energies of the valence orbitals of an ion in a crystal about the breaking of degeneracies of electron orbital states, usually d or f orbitals, which was developed by Hans Bethe, John Van Vleck, and Leslie Orgel.

For TiO₆ octahedral, each Ti-ion is surrounded by six O-ions arranged toward the corners of an octahedron. Therefore, a model for an *octahedral* complex in which a transition-metal ion is coordinated to six ligands. There are five-fold degeneracies for 3d orbital; the d_{xy} , d_{xz} , and d_{yz} orbitals in an octahedral complex are called the t_{2g} orbitals, and the $d_{x^2-y^2}$ and d_z^2 orbitals are called the e_g orbitals. The crystal field of the six O-ions splits the degeneracy of the five 3d orbitals. The energy of the five 3d orbitals increases when the six O-ions are brought close to the Ti-ion. However, the energy of two of these orbitals ($3d_{x^2-y^2}$ and $3d_z^2$) increases much more than the energy of the other three ($3d_{xy}$, $3d_{xz}$, and $3d_{yz}$), as shown in the figure 2.17 Therefore the difference between the energies of the t_{2g} and e_g orbitals in an octahedral complex is represented by the symbol (Δ_0). The magnitude of the splitting of the t_{2g} and e_g orbitals depends on the identity of the metal ion, the charge on this ion, and the nature of the ligands coordinated to the metal ion.

In SrTiO₃, the crystal field of the O-octahedron surrounding Ti splits the Ti3d bands into lower t_{2g} and higher e_g states. The lowest unoccupied conduction band consists of three empty t_{2g} bands which are degenerate at the Γ -point. While the higher e_g states consist of two band degeneracy. At low temperatures ($T < 105$ K), STO undergoes a structural phase transition to a tetragonally distorted structure and this degeneracy of the t_{2g} bands is lifted (Cowley, 1964).

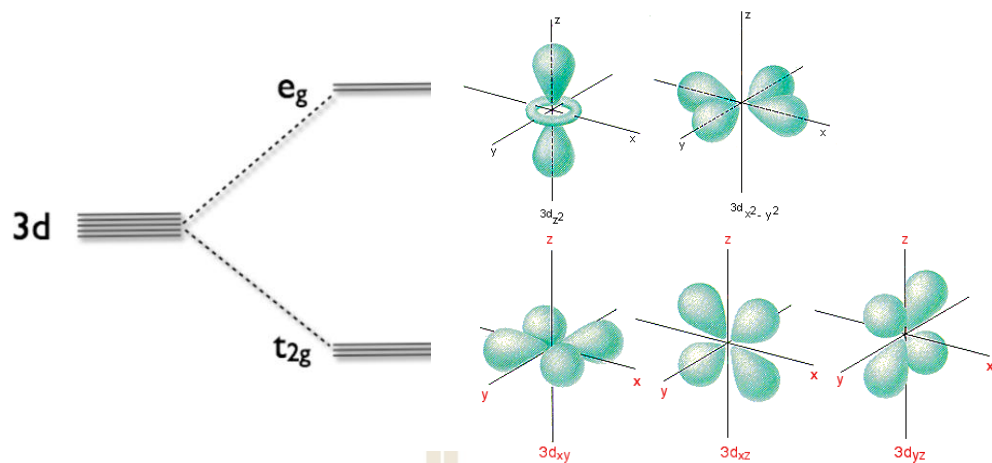


Figure 2.17 Schematic energy diagrams of the crystal field splitting and $3d$ orbital degeneracy. Two of the $3d$ orbitals on the Ti-ion point directly toward the six O ions. The other three orbitals ($3d_{xy}$, $3d_{xz}$, and $3d_{yz}$) lie between the O ions.

Salluzzo et al. (Salluzzo et al., 2009) found that the generation of a conducting electron gas related to an orbital reconstruction occurring at the $\text{LaAlO}_3/\text{SrTiO}_3$ interface and the degeneracy of the Ti $3d$ states is fully removed and the Ti $3d_{xy}$ levels become the first available states for conducting electrons, the Ti $3d_{yz}$ and Ti $3d_{zx}$ lift up levels of energy 50 meV as shown in figure 2.18.

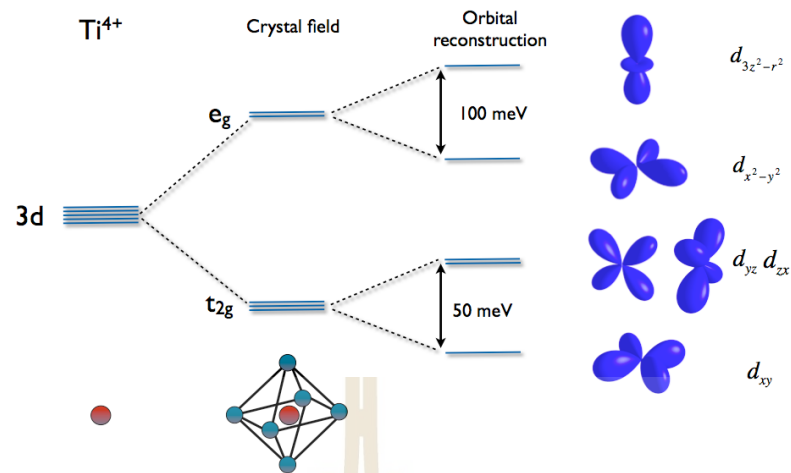


Figure 2.18 Schematic energy diagrams of the crystal field splitting and $3d$ orbital degeneracy, showing the orbital reconstruction at the interface and local bonding change. O_h denotes the octahedral environment (Salluzzo et al., 2009).

CHAPTER III

PHOTOEMISSION SPECTROSCOPY

Photoemission spectroscopy (PES) has unique advantage of directly probing band structure of materials. This technique is widely used for studying the single crystal solid materials. So, it is very important to understand the overall process of this spectroscopy. Here, in this chapter, we will introduce PES from its original view of photoelectric effect followed by the PES as well as angle-resolved photoemission spectroscopy (ARPES). We will introduce the simple physical pictures of photoemission process in section 3.3. The explanation of photoemission theory is described in section 3.4. The additional sections about the ARPES system and sample preparation are given in section 3.5 and 3.6, respectively.

3.1 Photoelectric effect

Photoemission spectroscopy (PES) is the technique which is used for probing the electronic structure of the materials based on the photoelectric effect. The photoelectric effect was discovered by Hertz in 1887 (Hertz, 1887) and was explained as the quantum nature of light by Einstein. While exposing the light with photon energy ($h\nu$), the electrons will be kicked out from the surface of the material with the minimum kinetic energy (E_{kin}) when the photon energy larger than work function (Φ). The kinetic energy ejected out of materials is depended on its binding energy (E_B) and whose relation can be written as

$$E_B = h\nu - \Phi - E_{kin} \quad (3.1)$$

In general, the work function of the analyzer (Φ_A) is larger than the measured sample ($\Phi_A > \Phi$), so in the experiment, we usually respect the Φ_A as the referenced work function defined for the Fermi level which can simply a lot in the experiment.

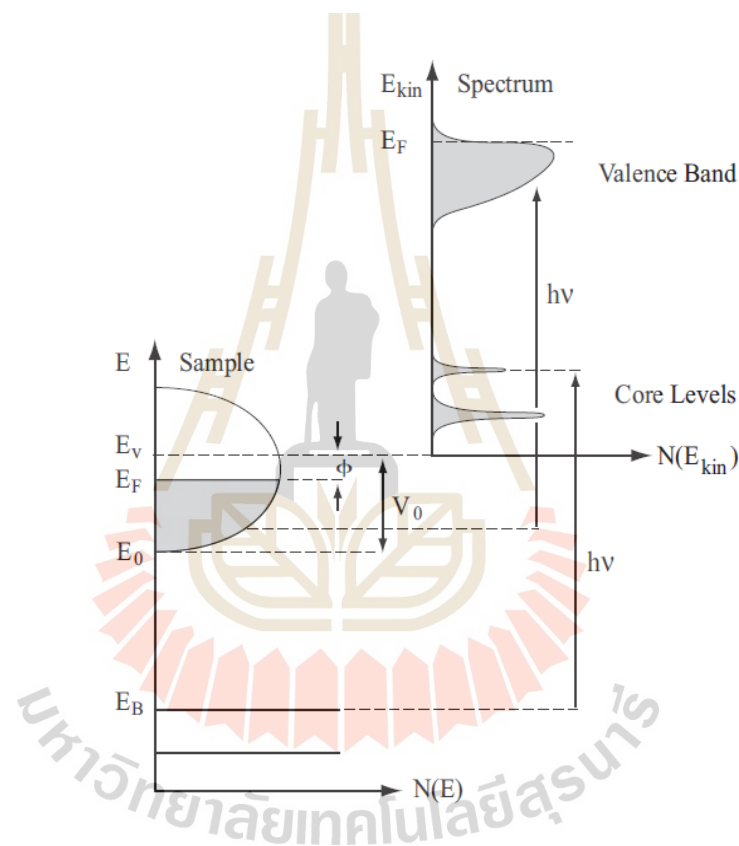


Figure 3.1 Illustration of the photoemission process where Fermi level (E_F), vacuum level (E_{vac}), work function of sample (Φ), kinetic energy of photoelectron (E_{kin}), binding energy (E_B) in material are represented in this model (Comin and Damascelli, 2013).

3.2 Photoemission spectroscopy

Irradiation of a material with photons of energy $h\nu$ releases electrons with kinetic energy E_{kin} from the surface if the energy of the light is larger than a characteristic value (work function) which depends on the material. The relation between kinetic energy of the electron and its binding energy E_B within the material can be determined via equation 3.1. More detailed parameters are shown in figure 3.1. Photoemission spectra are usually referenced with respect to the Fermi level in the sense that the Fermi level corresponds to zero binding energy. The range of accessible binding energies depends on the photon energy used for the excitation of the photoelectron. Photons in the vacuum ultraviolet (VUV) range are used for the excitation of valence electrons called ultraviolet photoemission spectroscopy (UPS), whereas soft x-rays can be used to excite core levels of materials called x-ray photoemission spectroscopy (XPS).

3.3 Angle-resolved photoemission spectroscopy (ARPES)

ARPES is a direct experimental technique to observe the distribution of the electrons in the reciprocal space of solids. This technique is one of the most direct methods of studying the electronic structure of the solid surfaces in the reciprocal space by giving information on the direction, speed and scattering process of valence electrons in the sample being studied (usually a solid) (Damascelli et al., 2002). This means that information can be gained on both the energy and momentum of an electron, resulting in detailed information on band dispersion and Fermi surface. This technique is a refinement of ordinary photoemission spectroscopy.

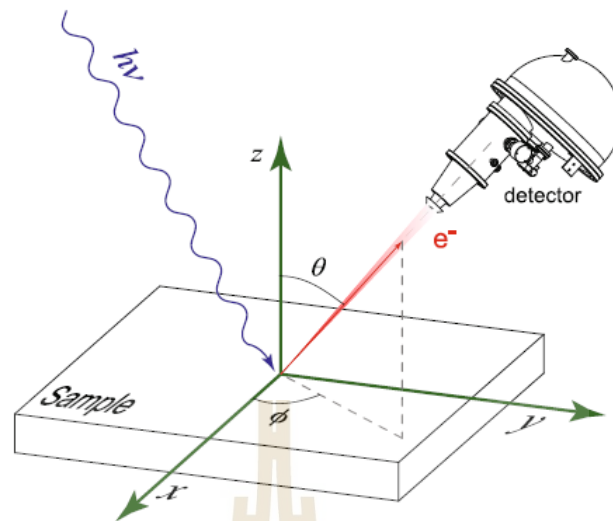


Figure 3.2 Schematic illustration of ARPES system, consisting of incident photon light, sample and analyzer (Zhang, 2013).

By measuring the kinetic energy and angular distribution of the photo-emitted electrons from a sample illuminated with sufficiently high-energy radiation, one can gain information on both the energy and momentum of the electrons propagating inside a material. This is of vital importance in elucidating the connection between electronic, magnetic, and chemical structure of solids, in particular for those complex systems which cannot be appropriately described within the independent-particle picture. The last decade witnessed significant progress in this technique and its applications, thus ushering in a new era in photoelectron spectroscopy. Nowadays, ARPES experiments with 2 meV energy and 0.28 angular resolutions are a reality even for photoemission on solids.

To determine the electronic structure in the materials which is simply shown in the relation of energy and momentum. From the photoelectric effect, kinetic energy of

ejected electrons from the sample excited from the light will be analyzed respected to the emission angle from the analyzer. As the in-plane momentum ($k_{//}$) is conserved in crystal surface, it can be determined from the emission angle (θ) (shown in figure 3.2) by this simple equation.

$$k_{//} = \sqrt{\frac{2m_e E_{kin}}{\hbar^2}} \sin\theta \quad (3.2)$$

In the past, to obtain such the momentum, we must rotate the angle every time to change the momentum as shown in figure 3.2. Fortunately, ARPES, the modern setup of PES, have been established with the line electron collector which can collect the electron in wide range of angle. This produces a lot of beneficial to shorten the experiment time in order of 1/1000 and makes the experiment much easier.

3.4 Photoemission process

The photoemission process can be simply described by following; after shining the light on the sample surface, electron will be ejected out by the photoelectric effect to the vacuum. From now on, using the energy and momentum conservation (eq. (3.1) and (3.2)) the behavior of these electrons can be determined. In the following part, we will give the appropriate and necessary description including three step model and the more realistic one step model which are shown in figure 3.3.

3.4.1 The three-steps model

The three-step model is the most intuitive approach to the photoemission process. Within the framework of this model the photoemission process is artificially split into three independent parts. The first step is the photoexcitation of the electron, where a

photon is absorbed and an electron-hole pair is created inside the crystal. The probability ω for this photoexcitation is given by Fermi's Golden Rule. In a second step, the electron propagates towards the crystal-vacuum interface. During this step the photoelectrons scatter with other electrons, plasmons or phonons, lose part of their energy and change their momentum. In the third step the electron is refracted at the crystal-vacuum interface and escapes through the surface. The measured photocurrent I is then proportional to the product of (i) the probability for the photoexcitation, (ii) the probability for the electron to arrive at the crystal-vacuum interface without being scattered, and (iii) the transmission function for the crystal-vacuum interface.

3.4.2 The one-step model

The separation of the photoemission process into three steps is artificial. The correct treatment of the photoemission process considers the whole process as one single step. The one-step model discusses the excitation from an initial state (Bloch state) into a damped final state near the surface. This damping takes care of the short mean free path of the electrons in a solid. In contrast to the three-step model, where the three processes are considered as being independent from each other, the one-step model takes into account interference between the three artificial steps. A correct one-step treatment of the photoemission process is based on Fermi's Golden Rule with proper functions for the initial and final state and the dipole operator for the interaction between electron and photon. This problem, however, cannot be solved rigorously. Various approximations have to be used to make a one-step calculation feasible. One of these approximations is the so-called sudden approximation which will be presented in the next paragraph.

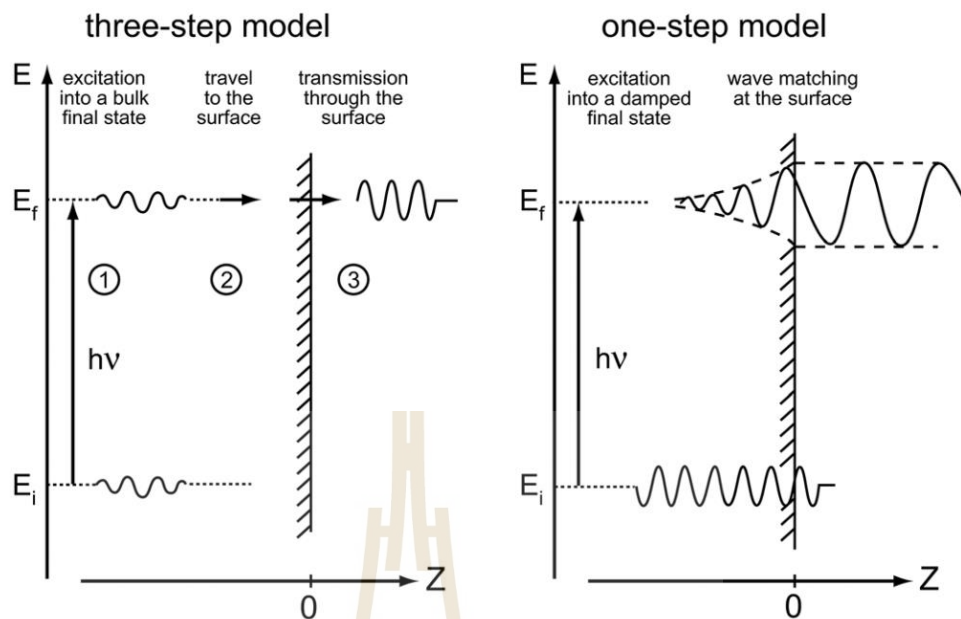


Figure 3.3 Three-step and one-step model description of the possible photoemission process (Hüfner, 1995).

3.5 Photoemission theory

This section will provide more intensive interpretation of photoemission after the simple physical picture of photoemission process has been presented in the previous section. Start with the very famous quantum physics rule called “Fermi’s golden rule”, which is used to approximate the probability of the transition from the N -electron ground state, into one of the possible final states by photoexcitation using the perturbation theory, the Fermi’s golden rule can be written as;

$$W_{fi} = \frac{2\pi}{\hbar} |\langle \Psi_f^N | H_{int} | \Psi_i^N \rangle|^2 \delta(E_f^N - E_i^N - h\nu) \quad (3.3)$$

Where E_i^N and E_f^N are the initial- and final- state energies of the N -particle system.

The photon field gives rise to photoemission via a perturbing term in the Hamiltonian given by

$$H_{int} = -\frac{e}{2mc} (\mathbf{2A} \cdot \mathbf{p} - i\hbar \nabla \cdot \mathbf{A}) \quad (3.4)$$

where \mathbf{p} is the electronic momentum operator and \mathbf{A} is the electromagnetic vector potential. In the bulk or continuous region, where \mathbf{A} is constant over atomic dimension, $\nabla \cdot \mathbf{A} = \mathbf{0}$. Then, the direct transition term, $\mathbf{A} \cdot \mathbf{p}$, exhibits dominant contribution to the photoemission intensity preserving the crystal momentum of the electron during the photoexcitation while the second term is ignored. However, at the surface, we should concern about $\nabla \cdot \mathbf{A}$ term which should be important where the electromagnetic field may have a strong spatial dependence and even be comparable to the direct transition term.

Next, the initial state wave function is assumed to be the product of one-electron orbital (ϕ_i^k), and an ($N-1$)-particle term from the single determinant expressed as

$$\Psi_i^N = A \phi_i^k \Psi_i^{N-1} \quad (3.5)$$

where A is the properly N -electron wave function antisymmetric operator, ϕ_i^k is the wave function of the initial state with momentum \mathbf{k} before photoexcitation, and Ψ_i^{N-1} is the wave function of the remaining ($N-1$) electrons.

Then the final state, within the sudden approximation can be also written as

$$\Psi_f^N = A \phi_f^k \Psi_f^{N-1} \quad (3.6)$$

ϕ_f^k is the wave function after photoexcitation, and Ψ_f^{N-1} is the final state wave function of the (N-1) electrons left behind.

Then substituting two above equations into eq.3.3, we can write:

$$\langle \Psi_f^N | H_{int} | \Psi_i^N \rangle = \langle \phi_f^N | H_{int} | \phi_i^k \rangle \langle \Psi_m^{N-1} | \Psi_i^{N-1} \rangle = M_{f,i}^k \langle \Psi_m^N | H_{int} | \Psi_i^N \rangle \quad (3.7)$$

where looking the final formula, $\langle \phi_f^N | H_{int} | \phi_i^k \rangle = M_{f,i}^k$ is the one-electron matrix element, the second term is the (N-1)-electron overlap integral, and the Ψ_f^{N-1} is replaced by the eigenstate (Ψ_m^{N-1}). The ejection of electron from ϕ_i^k to ϕ_f^k scatters the remaining (N-1) electrons system. The system will organize its minimum energy allowing many possible states with wave functions Ψ_s^{N-1} and energies E_s^{N-1} to be the final state of (N-1) electrons system. Then, the total photoemission intensity measured as a function of electron kinetic energy E_{kin} at a momentum \mathbf{k} , namely $I(k, E_{kin}) = \sum_{f,i} w_{f,i}$ will be equal to this expression:

$$I(k, E_{kin}) = \sum_{f,i} |M_{f,i}^k|^2 \sum_s |c_m|^2 \delta(E_{kin} + E_m^{N-1} - E_i^N - h\nu) \quad (3.8)$$

where $|c_m|^2 = |\langle \Psi_m^{N-1} | \Psi_i^{N-1} \rangle|^2$ is the probability that electron from initial state \mathbf{k} will be removed from (N-1) electrons systems into excited state \mathbf{s} . In non-interacting system, with $\Psi_i^{N-1} = \Psi_{m_0}^{N-1}$, for one particular $m = m_0$, which $|c_{m_0,i}|^2 = 1$ and all others is vanished, leading to ARPES spectra will be delta function at the Hartree-Fock orbital energy. In contrast, for strongly correlated systems, many of the $|c_{m,i}|^2$ will be non zero because in any Ψ_i^{N-1} will overlap with many of the eigenstates (Ψ_m^{N-1}). Hence, the ARPES spectra will not be the single but many delta functions according

the number of excited state created in the process. By invoking sudden approximation, we can now obtain the ARPES intensity for a 2D single-band system which can be written as:

$$I(\mathbf{k}, \omega) = I_0(\mathbf{k}, \nu, \mathbf{A})f(\omega)A(\mathbf{k}, \omega) \quad (3.9)$$

where $\mathbf{k}=\mathbf{k}_{//}$ is the in-plane electron momentum, ω is the electron energy respect to the Fermi level, ν is the electron energy, and \mathbf{A} is the polarization of incoming photon. Terms of $I_0(\mathbf{k}, \nu, \mathbf{A})$ is proportional to the squared one-electron matrix element ($|M_{f,i}^k|^2$), the Fermi dirac function, $f(\omega) = (e^{\omega/k_b T} + 1)^{-1}$ which probes only occupied states, and $A(\mathbf{k}, \omega)$ is already given as spectral function. In some case in many 2D systems, the $I_0(\mathbf{k}, \nu, \mathbf{A})$ is slowly varying respect to energy and momentum, photoemission can directly probe the spectral function which is directly related to the Green's function introduced by

$$A(\mathbf{k}, \omega) = -\frac{Im\{G(\mathbf{k}, \omega)\}}{\pi} \quad (3.10)$$

when correlated electron system, the correction to the Green function may be described in terms of electron self-energy $\Sigma(\mathbf{k}, \omega) = \Sigma'(\mathbf{k}, \omega) + i\Sigma''(\mathbf{k}, \omega)$. The real and imaginary parts of the self energy carry the information of the energy renormalization and lifetime of an electron with non-interacting band, $\varepsilon_{\mathbf{k}}$ and momentum \mathbf{k} . Thus, the Green's function can be expressed in term of self-energy as

$$G(\mathbf{k}, \omega) = \frac{1}{\omega - \varepsilon_{\mathbf{k}} - \Sigma(\mathbf{k}, \omega)} \quad (3.11)$$

Substituting eq. (3.11) to eq. (3.10), the corresponding spectral function is

$$A(k, \omega) = -\frac{1}{\pi} \frac{\Sigma''(k, \omega)}{[\omega - \varepsilon_k - \Sigma'(k, \omega)]^2 + [\Sigma''(k, \omega)]^2} \quad (3.12)$$

Note that ε_k is the bare band of the electron, we can see that when $\Sigma''(k, \omega) \rightarrow 0$, the spectral function is a delta function, or assuming no electron-electron correlation, the function will then be a Lorentzian function.

In general, many systems always have electron-electron correlation but remain at equilibrium itself. Disturbing the system by adding one extra electron into Bloch state will excite the whole system resulting in additional electron-hole pairs. Then all of energies and electron lifetimes are changed causing Fermi sea (discontinuous of momentum distribution). To simplify this matter, we introduce “quasiparticle” to describe the correlated electrons to be dressed by virtual excitations that move coherently with the electron through the crystal. Then, the spectral function in correlated electron system will now be determined by Lorentzian function based on energy and lifetime of introduced quasiparticle.

3.6 ARPES system and experimental detail

ARPES is one of the most direct methods for studying the electronic structure of solids. The electrons were emitted from a sample illuminated by sufficiently high energy radiation. This process can gain information on both the energy and momentum of the electrons propagating inside a material (Lindroos and Bansil, 1996; Zhang, 2013).

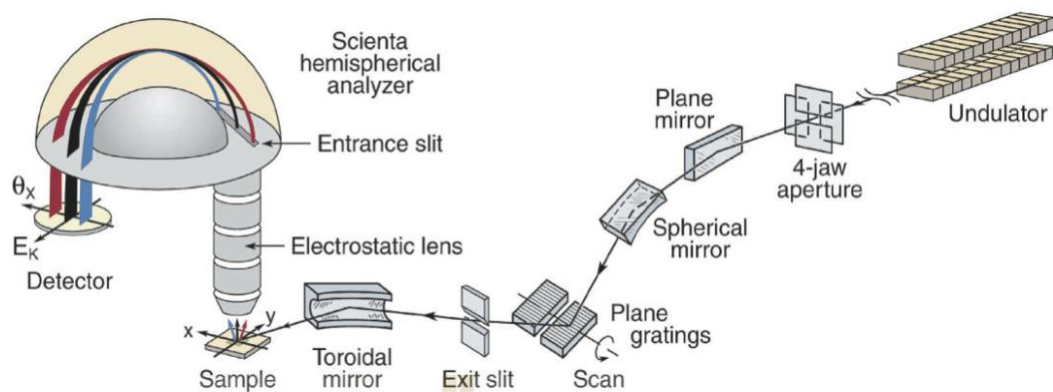


Figure 3.4 The diagram of beamline equipment consisted of a plane grating monochromator, optical slits, and electron analyzer (Damascelli, 2004).

There are two important components of ARPES system for high resolution measurement which are the light source and the electron analyzer. Nowadays, the development of both components together with the sample manipulating and cooling system gives the energy resolution in the order of < 10 meV which can be used to detect much of interesting physics phenomenon.

The synchrotron light source which contains wide spectral range of high intensity and continuous spectrum is commonly used for ARPES measurement. Other sources such as gas discharge lamps (monochromatic light with low intensity but high angular solution) and newly-developed lasers are also available. The synchrotron light radiation is generated by bending magnets holding electrons inside storage ring. The light is originated by controlling the classical electron dynamics states causing the charged particles by acceleration which emit electromagnetic radiation. In order to enhance the output of photon flux, many insertion devices such as wigglers or

undulators are installed along the storage ring until reaching the desired spot size. In ARPES, the multi-wavelength light passes through the grating for wavelength selection making the monochromatic photon (diagram is shown in figure 3.4).

The photon energy in ultraviolet (UV) regime is commonly used for surface sensitive ARPES due to the typical atomic-layer-mean-free-path. For synchrotron light (beamline resolution), the resolution is controlled by the exit slit before the sample. The electron analyzer is one of major components for ARPES consisting of an electrostatic lens, hemispherical detector, entrance slit, exit slit, and electron detector.

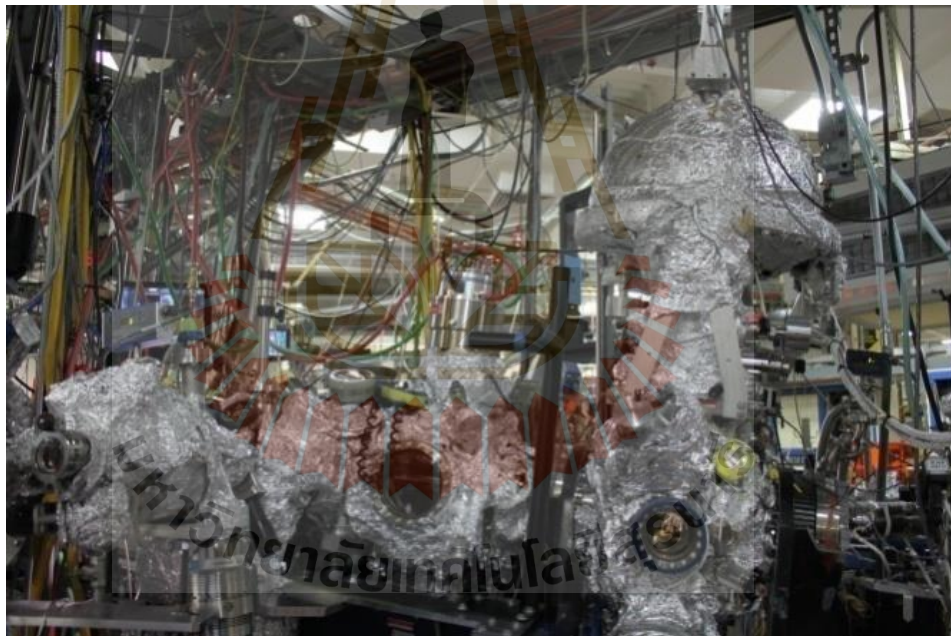


Figure 3.5 The high energy resolution ARPES at beamline 10.0.1 of the Advance Light Source, USA.

3.7 Sample preparation for ARPES measurement

Our samples are the single crystals of $\text{La}_x\text{Sr}_{1-x}\text{TiO}_3$ with $x=0.1\%$ with (110) (Crystal Base Co., Japan). The structural model of bulk SrTiO_3 (110), SrTiO_3 is a well-known transition metal oxide with a cubic perovskite structure at room temperature with lattice parameter $a = 3.905 \text{ \AA}$. It consists of two types of termination of $(\text{SrTiO})^{4+}$ and $(\text{O}_2)^{4-}$ surfaces. The 2D unit cell of $(\text{SrTiO})^{4+}$ surface is $a = 3.905 \text{ \AA}$ along k_z -direction or [001] and $b = 5.523 \text{ \AA}$ along k_M -direction or $[\bar{1}\bar{1}0]$ in real-space while, $k_z = 1.609 \text{ \AA}^{-1}$ and $k_m = 1.138 \text{ \AA}^{-1}$ in reciprocal (or k)-space as shown in figure 3.6.

To prepare the sample for measuring, first of all, we mounted our samples on the copper posts by Torr seal and ground them by using silver epoxy (EPOTEK H21) which is electrically conductive and vacuum compatible. Then, we checked the sample orientation and crystal structure by using Laue x-ray diffraction measurement (LAUE) with 25 kV and 20 mA. This step is very helpful to reduce the measuring time because the geometry and perfection of the sample (multiple or single domain) is revealed in this state. Figure 3.6 shows the example of the Laue-diffraction pattern of the STO(110) perfect crystal along Γ -X direction. After Laue measurement, we marked and pinned the sample direction with an alumina post for cleaving in UHV. After the sample is cleaved, we then take the ARPES experiments reported in this thesis were done by a Scienta-R4000 analyzer at the beamline 10.0.1 of the Advanced Light Source (ALS), USA. Real ARPES setup are shown in figure 3.5. The parameter used in our experiment are: photon energies between 50–60 eV and a pressure better than 10^{-11} torr. All ARPES data was measured with an energy resolution of 10-25 meV. Samples were cleaved at the measurement temperature of $T = 20 \text{ K}$ along (110) plane. Measurements were performed on stoichiometric transparent insulating samples as well as very lightly La-

doped samples ($\text{Sr}_{1-x}\text{La}_x\text{TiO}_3$ with $x = 0.001$) to help avoid charging. 2DEGs were induced at the bare surface by exposure to intense UV synchrotron light. The samples were exposed to irradiation doses more than $1,000 \text{ Jcm}^{-2}$ to saturate the formation of the 2DEG, and we experimentally confirmed that saturation was reached before starting any of the measurements.

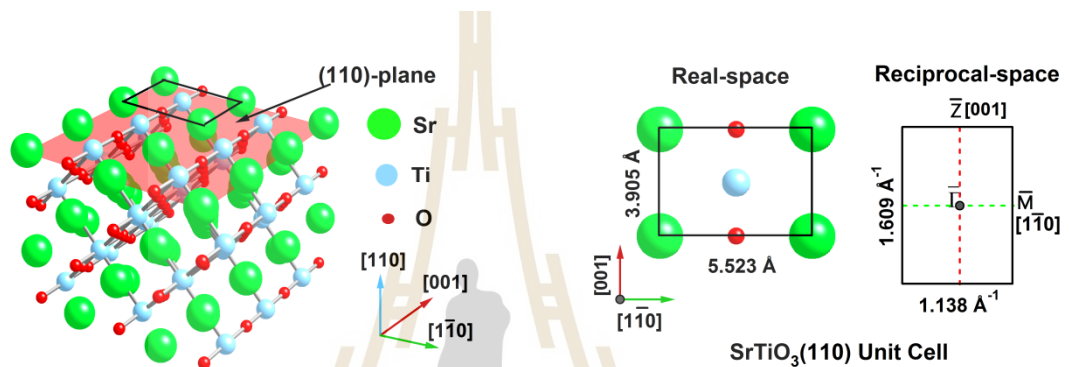


Figure 3.6 Crystal structure of $\text{SrTiO}_3(110)$, the 2D unit cell in real-space and reciprocal-space of $(\text{SrTiO})^{4+}$ surface.

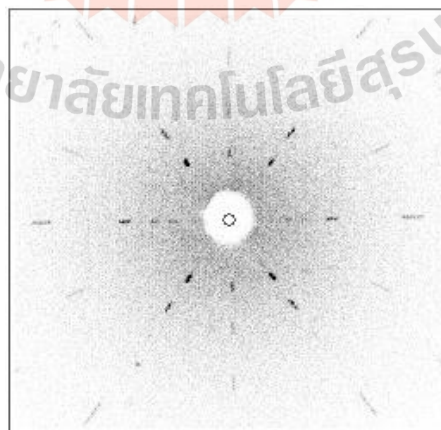


Figure 3.7 Laue pattern of STO (110) reflecting to the perfect rectangle shape with sharp spots.

CHAPTER IV

RESULTS AND DISCUSSIONS

In this chapter, we present the results of the electronic structure for La-doped SrTiO₃(110) surface after exposing the ultraviolet light by using the angle resolved photoemission spectroscopy (ARPES) technique. To study the valence band spectrum, particular the in-gap and 2DEG state, the band dispersion, the Fermi surface map (FSM), the effective mass (m^*), and the density of carriers (n). Finally, we discuss the results in term of the perspective of phenomena for density of carrier, application of the anisotropic effective mass for Seebeck coefficient enhancement, and comparison with the other results.

4.1 Experimental results of electronic structure

4.1.1 Valence band spectrum

By measuring ARPES data, the valence band spectrums mainly consist of two prominent oxygen $2p$ ($O2p$)-state which dominated in the binding energy range of 3-10 eV. After exposing the ultraviolet (UV) light of photon energy 50 eV and the photon intensity of 3.5 nA, the oxygen-vacancy state and 2DEG state were suddenly developed on a polar surface of SrTiO₃(110) at the in-gap and Fermi energy (E_F) level, respectively. The in-gap (or oxygen vacancy) state was induced at the peak of 1.1 eV approximately as shown in the figure 4.1.

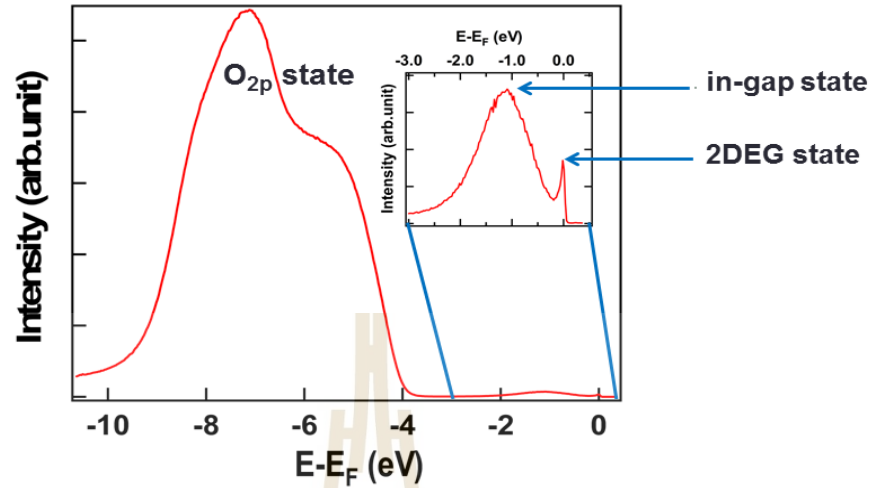


Figure 4.1 The valence band spectrum of oxygen $2p$ (O_{2p}) state between 3-10 eV, the in-gap state, and 2DEG state (inset) after exposing UV light.

4.1.2 Band dispersion

The band dispersion has shown in figure 4.2; (a) and (b) show the images of La-doped (110)-oriented SrTiO_3 surface which were measured in the direction of k_M at the Γ_{10} while (c) and (d) were measured in the direction of k_Z at the Γ_{11} for linear vertical polarized (p -pol) light and horizontal polarized (s -pol) light, respectively. We could observe at least 3 bands and the Fermi wave numbers (k_F) were different in crystalline direction. In k_M -direction, we could not observe the third band for the band dispersion measurement but we can approximate the k_F of the third band roughly $0.4\text{-}0.6 \text{ \AA}^{-1}$ from consideration the FSM (see figure 4.3(a) and (b)) which is the largest of k_F with heavy mass. The first band (the inner band of figure 4.2(a) or figure 4.2(b)) is strongly dispersion (lightly mass) but the second band is weakly dispersion (heavy mass) and the k_F of them were about 0.07 and 0.26 \AA^{-1} with have their bandwidths situated 0.054

eV and 0.068-0.126 eV below E_F , respectively. In k_z -direction, the first band (the outer band of figure 4.2(c) or figure 4.2(d)) is weakly dispersion (heavy mass), the k_F was about 0.33-0.36 \AA^{-1} and its bandwidths situated 0.051 eV while the second and the third bands were the strong dispersion (lightly mass) which k_F were about 0.09-0.10 and 0.13-0.16 \AA^{-1} and their bandwidths situated 0.073 eV and 0.104 eV below E_F , respectively.

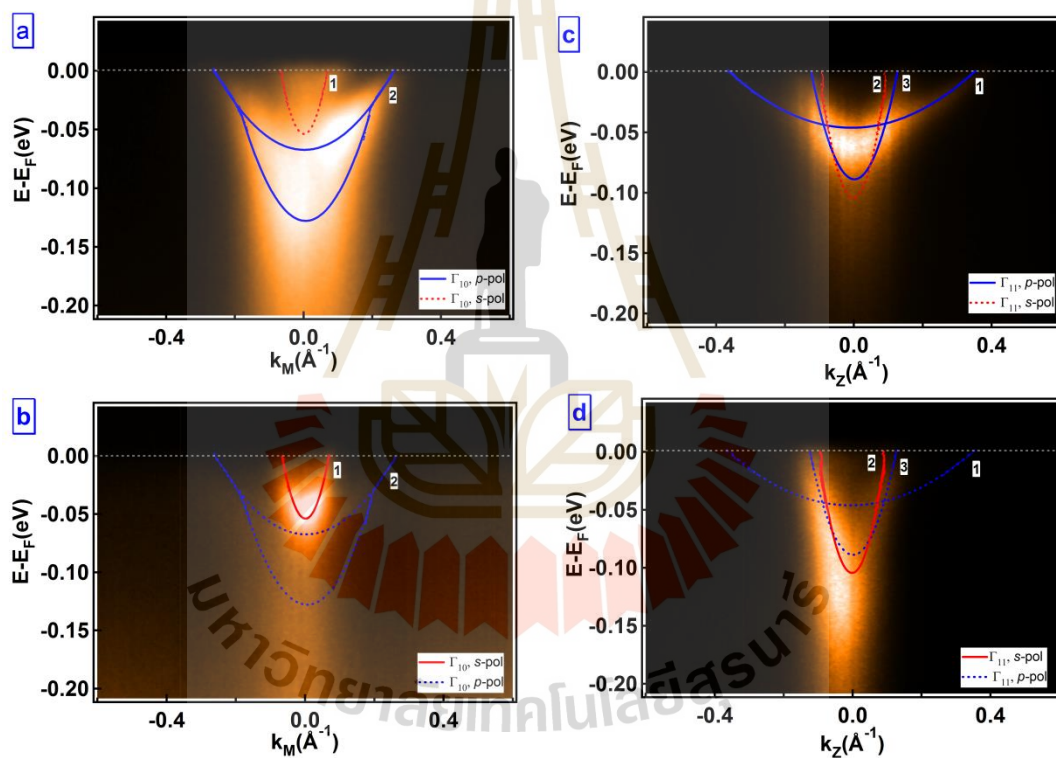


Figure 4.2 (a) and (b) show the band dispersion La doped (110)-oriented SrTiO_3 surface which were measured in the direction of k_M at the Γ_{10} while (c) and (d) in the direction of k_z at the Γ_{11} for p -pol and s -pol light.

We note that, at the Γ_{11} , it seems clearly to get the k_F both of three bands better than the Γ_{10} position. If we measure at the Γ_{11} in the k_M -direction may be will get the

band dispersion and the bandwidth of the third band. Moreover, we found that the energy of the weakly and strongly dispersion is lifted about 14-72 meV when measure in the k_M -direction, whereas the direction of k_Z , the weakly dispersion band is lower than the strong dispersion bands about 22-52 meV.

4.1.3 Fermi surface map (FSM)

The FSMs were shown as figure 4.3(a) and (d) for p-polarized light while figure 4.3(b) and 4.3(c) for p-polarized light. We note that, for S-polarized light, it seems to get k_F clearly only the inner band with was around 0.07 \AA^{-1} (see figure 4.3(a)) while for p- polarized light we could see both of the outer and inner bands with k_F around 0.26 and 0.07 \AA^{-1} , respectively (see figure 4.2(d)). The inner and outer-band widths were around 0.054 and 0.068 eV below the Fermi level, respectively. However, for cutting of this band, there were some shifts of the center of cutting then the k_F should be bigger, which were about 0.30 and 0.08 \AA^{-1} , respectively by using the extrapolation of Fermi surface map as shown in a summary of FSM in the figure 4.3(d). Finally, from the third FSM as shown in the figure 4.3(c), we could not observe the band dispersion in our measurement but we approximated the value of k_F about 0.40-0.60 \AA^{-1} from the mapping which has a large value of Fermi wave number (K_F) and may lead to a heavy effective mass.

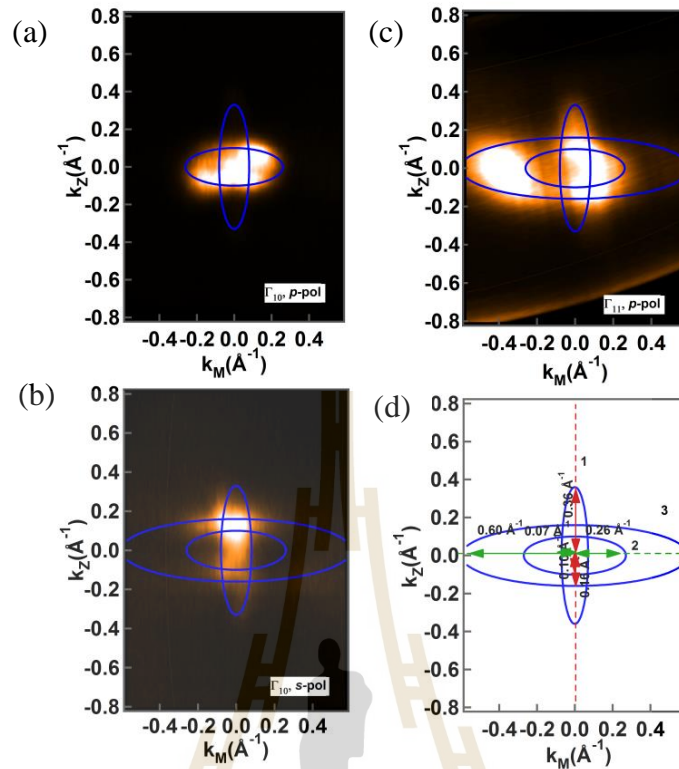


Figure 4.3 Fermi surface maps along the k_m -direction with p-polarized light (a) and s-polarized light (b) at the Γ_{10} -point, and along k_z -direction with p-polarized light at the Γ_{11} -point (c), momentum distribution curves with corresponding to (a-c) in figure 4.2, respectively, and (d) the schematic Fermi surface map of all (a-c).

4.1.4 Effective masses

In order to obtain the effective masses (m^*), we extracted the parabolic fits of the band dispersion (in figures 4.2) and calculated the effective mass from the relationship; $E_F = (\hbar^2 k_F^2)/2m^*$ by consideration both of the calculation of slope and coefficient of parabolic curve. The effective mass was different in crystallographic directions of [001] and $[1\bar{1}0]$. We could observe at least three bands with non-degenerate; a heavy ($m^* \cong (10-13)m_e$), a semi-heavy ($m^* \cong (1-2)m_e$), and a lightly ($m^* \cong 0.35m_e$), effective mass

along k_z or [001]-direction while a heavy ($m^* \cong (4.6-5.4)m_e$) and a lightly ($m^* \cong (0.3-0.4)m_e$) effective mass are observed along k_m or $[1\bar{1}0]$ -direction. Along the direction of k_z , a heavy effective mass is consistent with those from the 2DEG on the vacuum-cleaved surface of undoped SrTiO₃(001) (Santander-Syro et al., 2011) but a lightly effective mass differs from the vacuum-cleaved surface of La doped SrTiO₃ (100) by following as the same method ($m^* \cong (0.5 - 0.6)m_e$) (Meevasana et al., 2011).

Although the effective mass was anisotropic as the observation in the previous report of SrTiO₃(110) surface (Wang et al., 2014), there were differences in the value of our observation as shown in table 1. In particular, we got a large elliptic band ($k_F=0.4-0.6 \text{ \AA}^{-1}$ in directions of $[1\bar{1}0]$) of totally 3 bands, see figure 4.3(c), which could not be found in this report but we could not observe this band in the band dispersion as shown in figure 4.2(a) and (b).

4.1.4 Density of carriers

The total 2D-density of electron (n_{2D}) was defined from the number of electron in the Luttinger's area per area in the real-space. In this result, the Luttinger's area (A_L) can be determined from the all of three ellipsoid bands of the Fermi surface map as shown in the figure 4.3(d) consisting of an ellipsoid along k_z -direction with semi-axes of 0.07 and 0.33 \AA^{-1} and two ellipsoids along k_m -direction with semi-axes of 0.10 and 0.26 \AA^{-1} (the inner-band) and 0.16 and 0.60 \AA^{-1} (the outer-band), respectively. Then, the corresponding 2D carrier density was calculated; $n_{2D} = A_L/2\pi^2$ where $A_L = 54.42 \times 10^{14} \text{ cm}^{-2}$ which reach to the value of $2.34 \times 10^{14} \text{ cm}^{-2}$.

This value is slightly larger than the 2DEG densities observed at the vacuum-cleaved of La doped SrTiO₃ (100) surface ($8 \times 10^{13} \text{ cm}^{-2}$) (Meevasana et al., 2011),

undoped SrTiO₃(001) surface ($2 \times 10^{14} \text{ cm}^{-2}$) (Santander-Syro et al., 2011), and SrTiO₃(110) surface ($1.8 \times 10^{14} \text{ cm}^{-2}$) (Wang et al., 2014). The comparison of our observation and other previous works (e.g. Fermi wave number (k_F), bandwidth (E_w), effective mass (m^*) and density of carriers (n)) were shown in table 1 below.

Table 4.1 The comparisons of our observation between SrTiO₃ (110) and other orientations.

Orbital	SrTiO ₃ (100)/(001)		SrTiO ₃ (110)			
	Along k _X		Along k _Z		Along k _M	
	d _{yz}	d _{xy} /d _{zx}	d _{xy} (1 st -band)	d _{yz} /d _{zx} (2 nd /3 rd bands)	d _{yz} /d _{zx} (2 nd /3 rd bands)	d _{xy} (1 st -band)
K _F (Å ⁻¹)	- 0.3-0.4 _b	0.12, 0.175 ^a	0.40 ^d 0.36 ^e	0.11 ^d 0.10 ^e	0.34 ^d 0.26 ^e	0.10 ^d 0.07 ^e
E _w (eV)	- 0.040 ^b	0.21, 0.13 ^b 0.11, 0.216 ^a	0.062 ^d 0.051	0.16 ^e 0.072 ^d 0.104 ^e	0.4-0.6 ^e 0.072 ^d 0.068 ^e	0.062 ^d 0.054 ^e
m*(m _e)	- 10-20 ^b	0.100 ^b 0.5-0.6 ^a 0.7 ^a	9.7 ^d 10-13 ^e	0.67 ^d 1-2 ^e 0.35 ^e	6.1 ^d 4-6-5.4 ^e	0.74 ^d 0.3-0.4 ^e
n(cm ⁻²)	8x10 ¹³ (2 circle bands) ^a 2x10 ¹⁴ (a circle and 2 ellipsoid bands) ^b		1.89x10 ¹⁴ (2 ellipsoid bands) ^d 2.34 x10 ¹⁴ (3 ellipsoid bands) ^e			

^a (Meevasana et al., 2011), ^b (Santander-Syro et al., 2011), ^d (Wang et al., 2014), and ^e our results.

4.2 The calculation of band dispersion

To calculate the bands dispersion, we model the electronic structure using a tight-binding supercell with band bending included via additional on-site potential terms, similar to the method introduced by Stengel (Stengel, 2011). Figure 4.4 shows the band dispersion which was calculated by Barhamy (who is our collaborator at University of

Tokyo). It shows that the third band of our observation in the FSM image (see figure 4.3) may be possible with the Fermi wave number (k_F) about $0.4\text{-}0.6 \text{ \AA}^{-1}$ in direction of k_M and the bandwidth about $0.05\text{-}0.07 \text{ eV}$ but the first and the second bands are absent in our calculation. In the direction of k_Z , there are three bands of k_F about $0.8, 0.12,$ and 0.30 \AA^{-1} with the bottom energies of $0.02, 0.05,$ and 0.065 eV respectively while our observation in this direction shows that k_F 's are around $0.10, 0.16,$ and 0.36 \AA^{-1} with the bottom energies of $0.103, 0.073$ and 0.051 eV respectively.

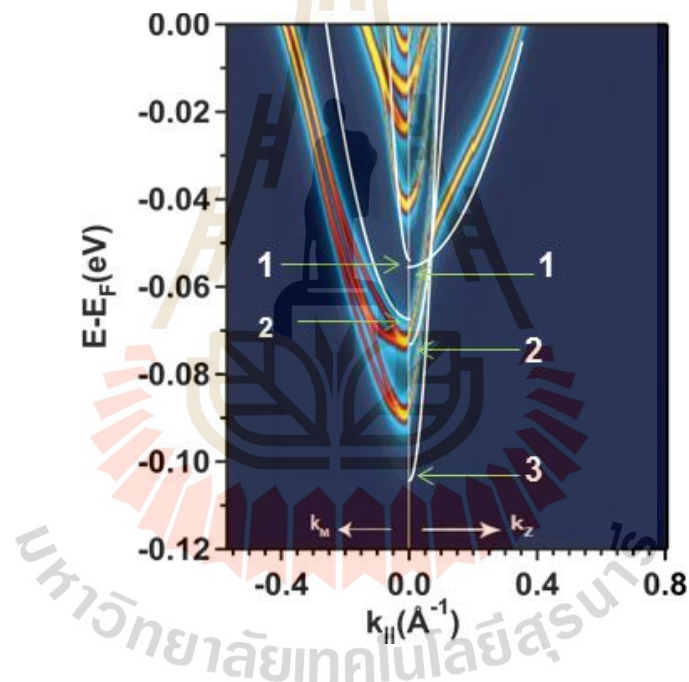


Figure 4.4 The band structure of $\text{SrTiO}_3(110)$ calculate by using a self-consistent tight-binding super cell compare to the experiment in the direction of k_M and k_Z (the white lines with labeled (1, 2, and 3) are ARPES data).

4.3 Discussion of the results

4.3.1 Effective mass and thermoelectric enhancement

The bulk single crystal of SrTiO₃ has been promising thermoelectric material because of 1) high effective mass, 2) the melting point of SrTiO₃ is 2080 °C, making it applicable at high temperature for thermoelectric materials (Ohta, 2007; Ohta et al., 2007), and 3) the electrical conductivity can be easily controlled by doping with La³⁺ or Nb⁵⁺ (Ohta et al., 2005). For example, La-doped SrTiO₃ has large power factor (PF) at room temperature (300 K), $PF = 3.6 \times 10^{-3} \text{ Wm}^{-1}\text{K}^{-2}$ (Okuda et al., 2001) while Nb-doped SrTiO₃ exhibits high thermoelectric figure of merit (ZT) about 0.37 at 1000K (Ohta et al., 2005).

Since the new direction for low-dimensional thermoelectric materials was predicted (Dresselhaus et al., 2007), there was a report of a new class of thermoelectric material of two-dimensional electron gas in SrTiO₃. It showed the giant thermoelectric Seebeck coefficient (S) with approximately five times larger than that of SrTiO₃ bulk. It was enhanced without reducing the electrical conductivity a factor of about 5 compared with the bulk and the figure of merit for thermoelectric performance (ZT) reached to 2.4, which is enhanced by a factor of 24 compared with the bulk of srTiO₃ and twice that of conventional thermoelectric material (Ohta, 2007; Ohta et al., 2007; Wood, 2007). Therefore, the existence of these anisotropic effective masses in our results indicate that 2DEG at (110)-oriented SrTiO₃ surface may use be a thermoelectric material application for enhancing the Seebeck coefficient (S) for switching of thermoelectric device.

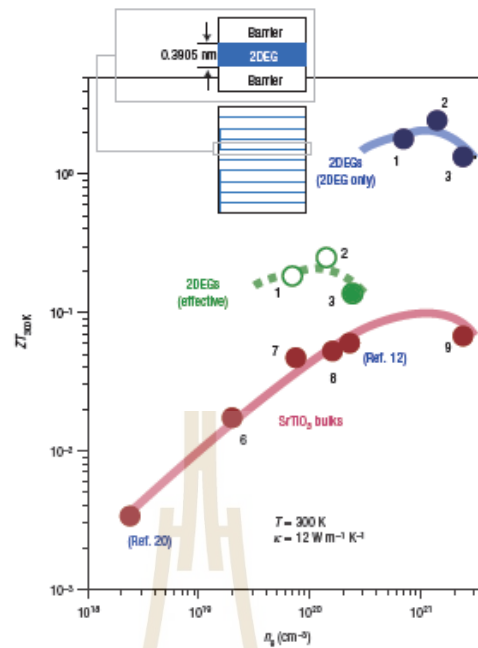


Figure 4.5 The thermoelectric figure of merit (ZT) of SrTiO_3 2DEG and bulk as a function of density of state (n_s) (Ohta et al., 2007).

4.3.2 Oxygen vacancy effect, density of carrier and perspective for Ferromagnetism

STO bulks are non-magnetic insulators but should be a metallic state by doping or having impurity which is lead to small distortion. For example, by doping La in Sr atom site ($\text{La}_{1-x}\text{Sr}_x\text{TiO}_3$), 2DEG is generated at $\text{SrTiO}_3(100)$ surface (Li and Yu, 2013). For the oxygen vacancy (OV) case, it is an important type of impurity defect in transition metal oxides (TMO). There are many experiments showing that oxygen vacancies contribute to the metallic state in STO surface and its interface. For example, OV are formed in the bulk STO substrate during the growth of LAO films, resulting in high electrical conductivity and mobility values (Kalabukhov et al., 2007). Moreover,

it causes strong atomic relaxation of the atoms around the vacancy site, thus reducing the octahedral symmetry of the crystal to tetragonal (Lue et al., 2004; Mitra et al., 2012).

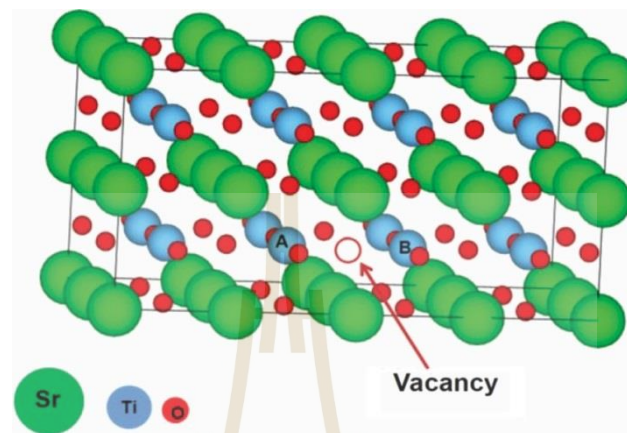


Figure 4.6 STO supercell containing oxygen vacancy (Mitra et al., 2012).

1) Oxygen vacancy induced reconstruction and 2DEG state

Shen et al. (Shen et al., 2012) studied the electronic structure of various oxygen-deficient $\text{SrTiO}_3(001)$ surface slabs using the density functional theory (DFT). The results found a significant surface reconstruction after introducing oxygen vacancies. The charges resulting from surface-localized oxygen vacancies redistribute in the surface region and deplete rapidly within a few layers from the surface suggesting the formation of a 2DEG. In figure 4.7, the number of electrons doped into the system due to the oxygen defect decreases from the surface to the bottom of the slab, and there is a dramatic drop after two layers for SrO termination and after only one layer for TiO_2 termination. This indicates that a two-dimensional electron gas (2DEG) forms at the surface.

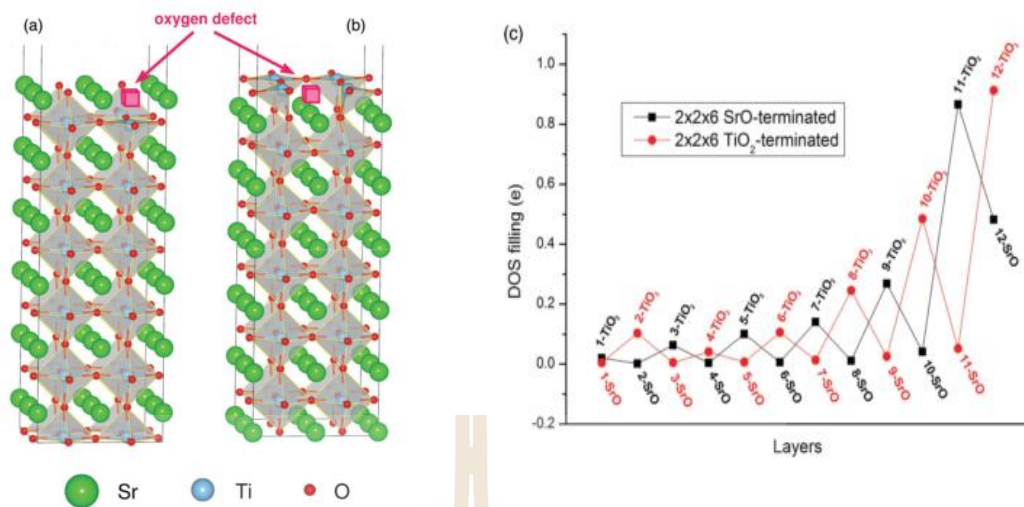


Figure 4.7 Structure of 2x2x6 SrTiO₃ slabs with oxygen vacancy in (a) the SrO and (b) TiO₂ Surface layer, and (c) the layer-decomposed electron filling of the gap states closed to the Fermi level as a function of depth. The layers are numbered from the bottom of the slab and the oxygen vacancy has been introduced on the top layer (Shen et al., 2012).

Moreover, OV introduced the 2DEG state and produces an in-gap state, peaked approximately 1.1 eV below the conduction band by ARPES measurement at temperature as low as 20 K and found that the OV concentration is proportional to the carrier density and thus suggesting that the vacancies are electron donor (Meevasana et al., 2011).

2) Oxygen vacancies introduce spin polarization and magnetism

Shein and Ivanovski (Shein and Ivanovskii, 2007) reported that oxygen and titanium vacancy introduce spin polarization of Ti and O atoms respectively around the defect site which lead to the magnetization of non-magnetic perovskite SrTiO₃.

Lin et al. (Lin and Demkov, 2013) studied the effect of oxygen vacancies in the lightly *n*-doped STO by consideration the electron correlation and explained that the oxygen vacancies can produce an in-gap state about 1 eV below the conduction band bottom. In addition, the oxygen vacancies should be fundamentally regarded as a magnetic impurity, due to the strong Coulomb repulsion, and may account for the observed interface ferromagnetism.

3) Density of state and perspective for ferromagnetism

Moreover, there was a recent theoretical model discussion about the 2DEG in SrTiO₃ surface to speculate the type of electronics properties which classified the density of carrier (*n*) into the three ranges (Khalsa and MacDonald, 2012); low-density ($n < 1 \times 10^{14} \text{ cm}^{-2}$), mid-range density ($1 \times 10^{14} \text{ cm}^{-2} < n < 5 \times 10^{14} \text{ cm}^{-2}$), and high density ($n > 5 \times 10^{14} \text{ cm}^{-2}$). The low density could exhibit the superconductivity while the mid and high density could exhibit the ferromagnetism which associate to the previous observation; 2DEG at the interface of LaAlO₃/SrTiO₃ (100) exhibited the superconducting and the increase in the density of the heavy 2D bands carrier could account for the ferromagnetism (Brinkman et al., 2007; Bert et al., 2011; Dikin et al., 2011; Li et al., 2011), our observation of the density of electron was in the mid-range density. This theory implies that the Rashba interaction with strong spin-orbit coupling are due to changes in metal-oxygen-metal bond angles and magneto transport properties which are strongly sensitive to local lattice polarization at the surface or interface (Khalsa et al., 2013).

Furthermore, there was a direct evidence of the ferromagnetic order at the interface of LaAlO₃/SrTiO₃ (100), with titanium (Ti³⁺) character in the *d_{xy}* orbital of the anisotropic *t_{2g}* band inducing by the electronic reconstruction (Lee et al., 2013).

This is a cause of the oxygen vacancy induced an orbital reconstruction and spin polarization which involve a lowering of the local symmetry and lead to the 2D-magnet state for titanate surfaces and interfaces (Pavlenko et al., 2012).

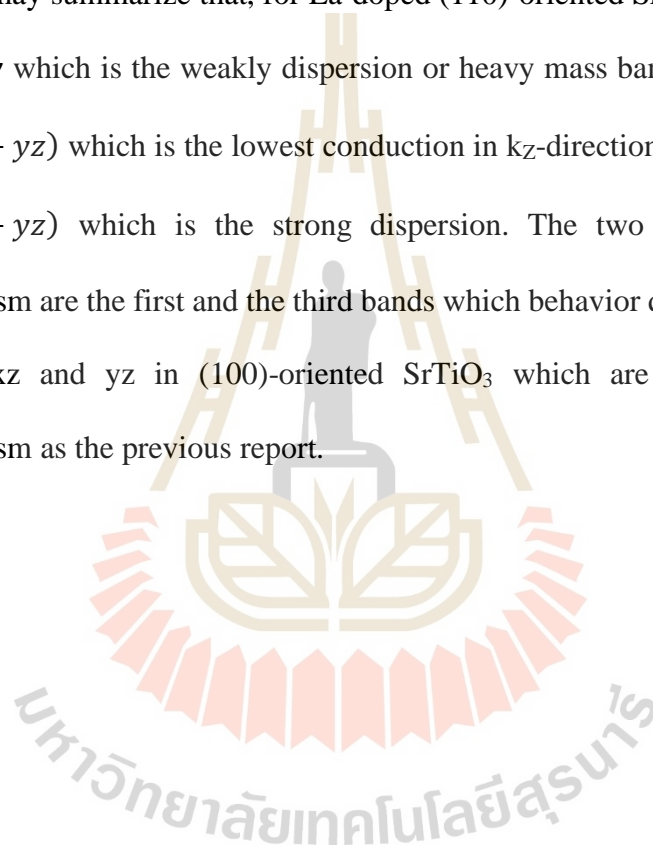
In addition, from consideration the electron correlation in oxygen vacancy in SrTiO₃, the oxygen vacancy should be as a magnetic impurity which effect on the lightly n-doped SrTiO₃ including interface ferromagnetism (Lin and Demkov, 2013).

Therefore, because these reasons and (110)-oriented SrTiO₃ has reconstructed easier than (100)-orientation, we expect that the ferromagnetism may be also observed at the surface La-doped (110)-oriented SrTiO₃. For discussion about the possibilities, we consider the previous observation on the ferromagnetism based on the (110)-oriented SrTiO₃; there was the report that the interface of (110)-oriented LaSrMnO₃/SrTiO₃ ultrathin superlattices exhibited stronger low-dimensional ferromagnetic and half-metallic (Ma et al., 2009; Zhu et al., 2011) and the magnetic properties of LaSrMnO₃/SrTiO₃ (110) films were enhanced than for (001) films which indicated that the spintronic devices with higher performance could be improved by using (110)-oriented SrTiO₃ substrate (Minohara et al., 2009).

Recently, the theoretical study proposed an unusual ferromagnetism in 2D-t_{2g} system which predict that SrTiO₃ (110) interface may emerge the ferromagnetism as SrTiO₃ (001) interface but should be absent in SrTiO₃ (111) interface. For SrTiO₃(001) interface with a fourfold rotation symmetry, a d_{xy} subband is the lowest energy and dispersion in 2D plane, while d_{xz} and d_{yz} subbands with degenerate are higher in energy and approximately 1D which is responsible for ferromagnetic polarization. Compared to (100) interface, the symmetry is reduced to a twofold rotation and the three t_{2g} orbitals are split into three non-degenerate orbitals; $1/\sqrt{2}(xz + yz)$, xy , $(1/\sqrt{2})(xz - yz)$.

The lowest band is $(1/\sqrt{2})(xz - yz)$ orbital and dispersion in 2D plane while $(1/\sqrt{2})(xz + yz)$ and xy orbitals are quasi-one-dimensional of t_{2g} bands in SrTiO_3 (110) which are not degenerate, there may even exist two ferromagnetic regimes as the electron filling of the upper subband is increased (Chen and Balents, 2013).

To compare this explanation with our band dispersions with non-degenerate orbitals, we may summarize that, for La-doped (110)-oriented SrTiO_3 , the first band is the orbital xy which is the weakly dispersion or heavy mass band, the second band is $(1/\sqrt{2})(xz - yz)$ which is the lowest conduction in k_z -direction, and the third band is $(1/\sqrt{2})(xz + yz)$ which is the strong dispersion. The two bands that effect to ferromagnetism are the first and the third bands which behavior quasi-1D bands like as the orbital xz and yz in (100)-oriented SrTiO_3 which are 1D and respond to ferromagnetism as the previous report.



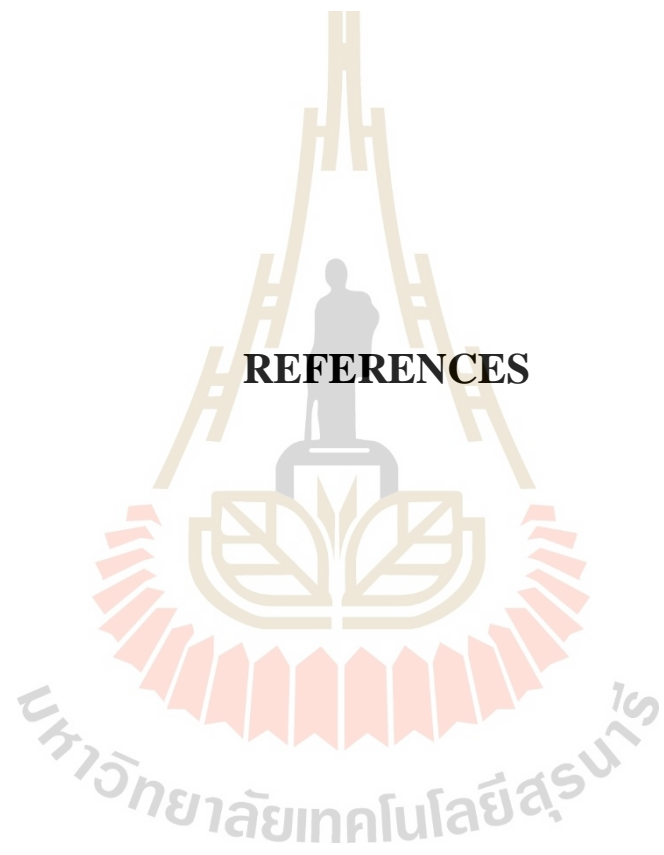
CHAPTER V

CONCLUSIONS

5.1 Conclusions

This work presents the in-depth electronic structure of SrTiO₃(110) studied by Angle-resolved photoemission spectroscopy (ARPES). We reported the valence band spectrum including O_{2p} and oxygen vacancy states essentially to the formation of two-dimensional electron gases (2DEGs). Band dispersion, derivation of Fermi wave vector (K_F) and the Fermi surface map (FSM) along K_Z and K_M have been demonstrated using linear vertical (LV) and linear horizontal (LH) polarization. We can conclude that there are three anisotropic bands denoted as heavy, semi-heavy, and lightly bands. Those bands have effective masses of around 10, 1.5, and 0.35 of the electron masses. The maximum carrier densities have been calculated as high as $2.34 \times 10^{14} \text{ cm}^{-2}$. The difference behavior between SrTiO₃(110) and SrTiO₃(100) have been demonstrated which is suggested to different potential application. The role of oxygen vacancy in the aspect of surface reconstruction, spin polarization and magnetism have been purposed. We have also performed the tight binding calculation which is well in agreement to our experimental data. Finally, we have shown the relation between effective masses and carrier densities to thermoelectric and ferromagnetic application.

REFERENCES



REFERENCES

- Annadi, A., Zhang, Q., Renshaw Wang, X., Tuzla, N., Gopinadhan, K., Lü, W. M., Roy Barman, A., Liu, Z. Q., Srivastava, A., Saha, S., Zhao, Y. L., Zeng, S. W., Dhar, S., Olsson, E., Gu, B., Yunoki, S., Maekawa, S., Hilgenkamp, H., Venkatesan, T., and Ariando. (2014). Anisotropic two-dimensional electron gas at the $\text{LaAlO}_3/\text{SrTiO}_3$ (110) interface. **Nat. Comm.** 4: 1838.
- Bert, J. A., Kalisky, B., Bell, C., Kim, M., Hikita, Y., Hwang, H. Y., and Moler, K. A. (2011). Direct imaging of the coexistence of ferromagnetism and superconductivity at the $\text{LaAlO}_3/\text{SrTiO}_3$ interface. **Nature Phys.** 7: 767.
- Brinkman, A., Huijben, M., van Zalk, M., Huijben, J., Zeitler, U., Maan, J. C., van der Wiel, W. G., Rijnders, G., Blank, D. H. A., and Hilgenkamp, H. (2007). Magnetic effects at the interface between non-magnetic oxides. **Nat. Mater.** 6: 493.
- Cardona, M. (1965). Optical properties and band structure of SrTiO_3 and BaTiO_3 . **Phys. Rev.** 140(2A): A651.
- Caviglia, A. D., Gariglio, S., Reyren, N., Jaccard, D., Schneider, T., Gabay, M., Thiel, S., Hammerl, G., Mannhart, J., and Triscone, J.-M. (2008). Electric field control of the $\text{LaAlO}_3/\text{SrTiO}_3$ interface ground state. **Nature.** 456: 624.
- Cen, C., Thiel, S., Mannhart, J., and Levy, J. (2009). Oxide Nanoelectronic on Demand. **Science.** 323: 1026.

- Chaudhari, P., Koch, R. H., Laibowitz, R. B., McGuire, T. R., and Gambino, R. J. (1987). Critical-current measurements in epitaxial films of YBa_2Cu . **Phys. Rev. Lett.** 58(25): 2684.
- Chen, G., and Balents, L. (2013). Ferromagnetism in Itinerant Two-Dimensional t_{2g} Systems. **Phys. Rev. Lett.** 110: 206401.
- Comin, R., and Damascelli, A. (2013). ARPES: A probe of electronic correlations. **arXiv:** 1303v.
- Cowley, R. A. (1964). Lattice dynamics and phase transition of strontium titanate. **Phys. Rev.** 134: A981.
- Damascelli, A., Shen, Z.-X., and Hussain, Z. (2002). Angle-resolved photoemission spectroscopy of the cuprate superconductors. **arXiv:** 208504v.
- Damascelli, A. (2004). Probing the electronic structure of complex systems by ARPES. **Phys. Scripta.** T109: 61.
- Dikin, D. A., Mehta, M., Bark, C. W., Folkman, C. M., Eom, C. B., and Chandrasekhar, V. (2011). Coexistence of superconductivity and ferromagnetism in two dimensions. **Phys. Rev. Lett.** 107: 056802.
- Dresselhaus, M. S., Chen, G., Tang, M. Y., Yang, R. G., Lee, H., Wang, D. Z., and Gogna, P. (2007). New Directions for Low-Dimensional Thermoelectric Materials. **Adv. Mater.** 19(8): 1043.
- Fleury, P. A., Scott, J. F., and Worlock, J. M. (1968). Soft Phonon Modes and the 110°K Phase Transition in SrTiO_3 . **Phys. Rev. Lett.** 21(1): 16.
- Gabay, M., Gariglio, S., Triscone, J.-M., and Santander-Syro, A. F. (2013). 2-Dimensional oxide electronic gases: Interfaces and surfaces. **Eur. Phys. J. Spec. Top.** 222(5): 1177.

- Hertz, H. (1987). Ueber den Einfluss des ultravioletten Lichtes auf die electriche Entladung. **Ann.Phys.** 267: 983.
- Herranz, G., Basletić, M., Bibes, M., Carrétéro, C., Tafrá, E., Jacquet, E., Bouzouane, K., Deranlot, C. Hamzić, A., Broto, J.-M, and Barthélémy, A., and Fert, A. (2007) . High Mobility in LaAlO₃/ SrTiO₃ heterostructures: Origin, dimensionality, and perspectives. **Phys. Rev. Lett.** 98: 216803.
- Herranz, G., Bergeal, N., Lesueur, J., Gazquez, J., Scigaj, M., Dix, N., Sanchez, F., and Fontcuberta, J. (2013). Orientational tuning of the 2D- superconductivity in LaAlO₃/SrTiO₃ interfaces. **arXiv:** 1305.2411v1.
- Herranz, G., Sánchez, F., Dix, N., Scigaj, M., and Fontcuberta, J. (2012). High mobility conduction at (110) and (111) LaAlO₃/SrTiO₃ interfaces. **Sci. Rep.** 2: 758.
- Hosoda, M., Hikita, Y., Hwang, H. Y., and Bell, C. (2013). Transistor operation and mobility enhancement in top- gated LaAlO₃/ SrTiO₃ heterostructures. **Appl. Phys. Lett.** 103: 103507.
- Huijben, M., Rijnders, G., Blank, D. H. A., Bals, S., Van Aert, S., Verbeeck, J., Van Tendeloo, G., Brinkman, A., and Hilgenkamp, H. (2006) . Electronically coupled complementary interfaces between perovskite band insulators. **Nat. Mater.** 5: 556.
- Hüfner, S. (1995). **Photoemission spectroscopy**. Berlin: Springer-Verlag.
- Hwang, H. Y., Iwasa, Y., Kawasaki, M., Keimer, B., Nagaosa, N., and Tokura, Y. (2012). Emergent phenomena at oxide interfaces. **Nat. Mater.** 11: 103.
- Itoh, M., Wang, R., Inaguma, Y., Yamaguchi, T., Shan, Y.-J., and Nakamura, T. (1999). Ferroelectricity Induced by Oxygen Isotope Exchange in Strontium Titanate Perovskite **Phys. Rev. Lett.** 82(17): 3540.

- Kahn, A. H., and Leyendecker, J. (1964). Electronic Energy Bands in Strontium Titanate **Phys. Rev.** 135(5A): A1321.
- Kalabukhov, A., Gunnarsson, R., Börjesson, J., Olsson, E., Claeson, T., and Winkler, D. (2007). Effect of oxygen vacancies in the SrTiO₃ substrate on the electrical properties of the LaAlO₃/SrTiO₃ interface **Phys. Rev. B.** 75: 121404(R).
- Khalsa, G., Lee, B., and MacDonald, A. H. (2013). Theory of t_{2g} electron-gas Rashba interactions. **Phys. Rev. B.** 88(4): 041302.
- Khalsa, G., and MacDonald, A. H. (2012). Theory of the SrTiO₃ surface state two-dimensional electron gas. **Phys. Rev. B.** 86(12): 125121.
- King, P. D. C., Walker, S. M., Tamai, A., de la Torre, A., Eknapakul, T., Buaphet, P., Mo, S.-K., Meevasana, W., Bahramy, M. S., and Baumberger, F. (2014). Quasiparticle dynamics and spin-orbital texture of the SrTiO₃ two-dimensional electron gas. **Nat. Comm.** 5: 3414.
- Kohn, W., and Sham, L. J. (1965). Self-Consistent Equations Including Exchange and Correlation Effects. **Phys. Rev.** 140(4A): A1133.
- Lee, J. H., Fang, L., Vlahos, E., Ke, X., Jung, Y. W., Kourkoutis, L. F., Kim, J. W., Ryan, P. J., Heeg, T., Roeckerath, M., Goian, V., Bernhagen, M., Uecker, R., Hammel, P. C., Rabe, K. M., Kamba, S., Schubert, J., Freeland, J. W., Muller, D. A., Fennie, C. J., Schiffer, P. Gopalan, V., Halperin, E. J., and Schlom, D. G. (2010). A strong ferroelectric ferromagnet created by means of spin-lattice coupling. **Nature.** 466: 954.
- Li, L., Richter, C., Mannhart, J., and Ashoori, R. C. (2011). Coexistence of magnetic order and two-dimensional superconductivity at LaAlO₃/SrTiO₃ interfaces. **Nature Phys.** 7: 762.

- Li, L., Richter, C., Paetel, S., Kopp, T., Mannhart, J., and Ashoori, R. C. (2011). Very large capacitance enhancement in a two-dimensional electron system. **Science**. 332: 825.
- Li, Y., and Yu, J. (2013). Two-dimensional electron gas generated by La-doping at SrTiO₃(001) surface: A first-principles study. **AIP Adv.** 3: 062116.
- Lin, C., and Demkov, A. A. (2013). Electron correlation in oxygen vacancy in SrTiO₃. **Phys. Rev. Lett.** 111: 217601.
- Lindroos, M., and Bansil, A. (1996). A Novel Direct Method of Fermi Surface Determination Using Constant Initial Energy Angle-Scanned Photoemission Spectroscopy. **Phys. Rev. Lett.** 77(14): 2985.
- Liu, Z. Q., Li, C. J., Lü, W. M., Huang, X. H., Huang, Z., Zeng, S. W., Qiu, X. P., Huang, L. S., Annadi, A., Chen, J. S., Coey, J. M. D., Venkatesan, T., and Ariando. (2013). Origin of the two-dimensional electron gas at LaAlO₃/SrTiO₃ interfaces: the role of oxygen vacancies and electronic Reconstruction. **Phys. Rev. X**. 3: 021010.
- Lue, W., Duan, W., Louie, S. G., and Cohen, M. L. (2004). Structural and electronic properties of n-doped and p-doped SrTiO₃. **Phys. Rev. B**. 70: 214109.
- Ma, J. X, Liu, X. F., Lin, T., Gao, G. Y., Zhang, J. P., Wu, W. B., Wu, X. G. and Shi, J. (2009). Interface ferromagnetism in (110)-oriented La_{0.7}Sr_{0.3}MnO₃/SrTiO₃ ultrathin superlattices. **Phys. Rev. B**. 79: 174424
- Mattheiss, L. F. (1972a). Effect of the 110 °K phase transition on the SrTiO₃ conduction bands. **Phys. Rev. B**. 6(12): 4740.
- Mattheiss, L. F. (1972b). Energy Bands for KNiF₃, SrTiO₃, KMnO₃, and KTaO₃. **Phys. Rev. B**. 6(12): 4718.

- Meevasana, W., King, P. D. C., He, R.-H., Mo, S.-K., Hashimoto, M., Tamai, A., Songsiriritthigul, P., Baumberger, F., and Shen, Z.-X. (2011). Creation and control of a two-dimensional electron liquid at the bare SrTiO₃ surface. **Nat. Mater.** 10: 114.
- Minohara, M., Furukawa, Y., Yasuhara, R., Kumigashira, H., and Oshima, M. (2009). Orientation dependence of the Schottky barrier height for La_{0.6}Sr_{0.4}MnO₃/SrTiO₃ heterojunctions. **Appl. Phys. Lett.** 94: 242106.
- Mitra, C., Lin, C., Robertson, J., and Demkov, A. A. (2012). Electronic structure of oxygen vacancies in SrTiO₃ and LaAlO₃. **Phys. Rev. B.** 86: 155105.
- Nakagawa, N., Hwang, H. Y., and Muller, D. A. (2006). Why some interface cannot be sharp **Nat. Mater.** 5: 204.
- Noland, J. A. (1954). Optical absorption of single-crystal Strontium titanate. **Phys. Rev.** 94: 724.
- Ohta, H. (2007). Thermoelectrics based on strontium titanate. **Mater. Today.** 10: 44.
- Ohta, H., Kim, S., Mune, Y., Mizoguchi, T., Nomura, K., Ohta, S., Nomura, T., Nakanishi, Y., Ikuhara, Y., Hirano, M., Hosono, H., and Koumoto, K. (2007). Giant thermoelectric Seebeck coefficient of a two-dimensional electron gas in SrTiO₃. **Nat. Mater.** 6: 129.
- Ohta, H., Mizuno, T., Zheng, S., Kato, T., Ikuhara, Y., Abe, K., Abe, K., Kumomi, H., Nomura, K., and Hosono, H. (2012). Unusually large enhancement of thermopower in an electric field induced two-dimensional electron gas. **Adv. Mater.** 24: 740

- Ohta, H. (2013). Electric-field thermopower modulation in SrTiO₃-based field-effect transistors. **J. Mater. Sci.** 48: 2797.
- Ohtomo, A., and Hwang, H. Y. (2004). A high-mobility electron gas at the LaAlO₃/SrTiO₃ heterointerface. **Nature London.** 427: 423.
- Ohta, S., Nomura, T., Ohta, H., Hirano, M., Hosono, H., and Koumoto, K. (2005). Large thermoelectric performance of heavily Nb-doped SrTiO₃ epitaxial film at high temperature. **Appl. Phys. Lett.** 87: 092108.
- Ohta, S., Nomura, T., Ohta, H., and Koumoto, K. (2005). High-temperature carrier transport and thermoelectric properties of heavily La- or Nb-doped SrTiO₃ single crystals. **J. Appl. Phys.** 97: 034106.
- Okuda, T., Nakanishi, K., Miyasaka, S., and Tokura, Y. (2001). Large thermoelectric response of metallic perovskites: Sr_{1-x}La_xTiO₃ (0 < x < 0.1). **Phys. Rev. B.** 63: 113104.
- Orhan, E., Pontes, F. M., Pinheiro, C. D., Boschi, T. M., Leite, E. R., Pizani, P. S., Beltran, A., Andres, J., Varela, J.A., and Longo, E. (2004). Origin of photoluminescence in SrTiO₃: a combined experimental and theoretical study. **J. Sol. Stat. Chem.** 177: 3879.
- Pavlenko, N., Kopp, T., Tsymbal, E. Y., Mannhart, J., and Sawatzky, G. A. (2012). Oxygen vacancies at titanate interfaces: Two-dimensional magnetism and orbital reconstruction. **Phys. Rev. B.** 86: 064431
- Reyren, N., Thiel, S., Cavaglia, A. D., Kourkoutis, L. F., Hammerl, G., Richter, C., Schneider, C. W., Kopp, T., Rüetschi, A.-S., Jaccard, D., Gabay, M., Müller, D. A., Triscone, and J.-M., Mannhart, J. (2007). Superconducting interfaces between insulating oxides. **Science.** 317: 1196.

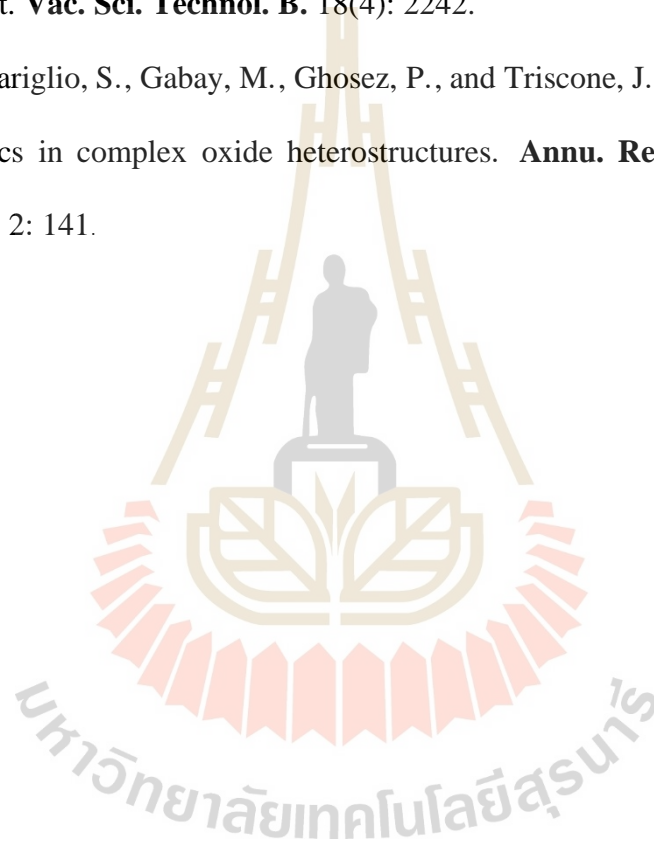
- Salluzzo, M., Cezar, J. C., Brookes, N. B., Bisogni, V., De Luca, G. M., Richter, C., Thiel, S., Mannhart, J., Huijben, M., Brinkman, A., Rijnders, G., and Ghiringhelli, G. (2009). Orbital reconstruction and the two-dimensional electron gas at the $\text{LaAlO}_3/\text{SrTiO}_3$ interface. **Phys. Rev. Lett.** 102: 166804.
- Santander-Syro, A. F., Copie, O., Kondo, T., Fortuna, F., Pailhès, S., Weht, R., Qiu, X. G., Bertran, F., Nicolaou, A., Taleb-Ibrahimi, A., Le Fèvre, P., Herranz, G., Bibes, M., Reyren, N., Apertet, Y., Lecoœur, P., Barthélémy, A., and Rozenberg, M. J. (2011). Two-dimensional electron gas with universal subbands at the surface of SrTiO_3 . **Nature.** 469: 189.
- Shein, I. R. A., and Ivanovskii, L. (2007). First principle prediction of vacancy-induced magnetism in non-magnetic perovskite SrTiO_3 . **Phys. Lett. A.** 371: 155.
- Shen, J., Lee, H., Valentí, R., and Jeschke, H. O. (2012). Ab initio study of the two-dimensional metallic state at the surface of SrTiO_3 : Importance of oxygen vacancies. **Phys. Rev. B.** 86: 195119.
- Siemons, W., Koster, G., Yamamoto, H., Harrison, W. A., and Lucovsky, G. (2007). Origin of charge density at LaAlO_3 on SrTiO_3 heterointerfaces: possibility of intrinsic doping. **Phys. Rev. Lett.** 98: 196802.
- Skinner, B., and Shklovskii, B. I. (2010). Anomalously large capacitance of a plane capacitor with a two-dimensional electron gas. **Phys. Rev. B.** 82: 155111.
- Smits, F. M. (1957). Measurement of sheet resistivity with the four point probe. **The Bell Sys. Tech. J.** May: 717.
- Stemmer, S., and Allen, S. J. (2014). Two-dimensional electron gases at complex oxide interfaces. **Annu. Rev. Mater. Res.** 44: 151.

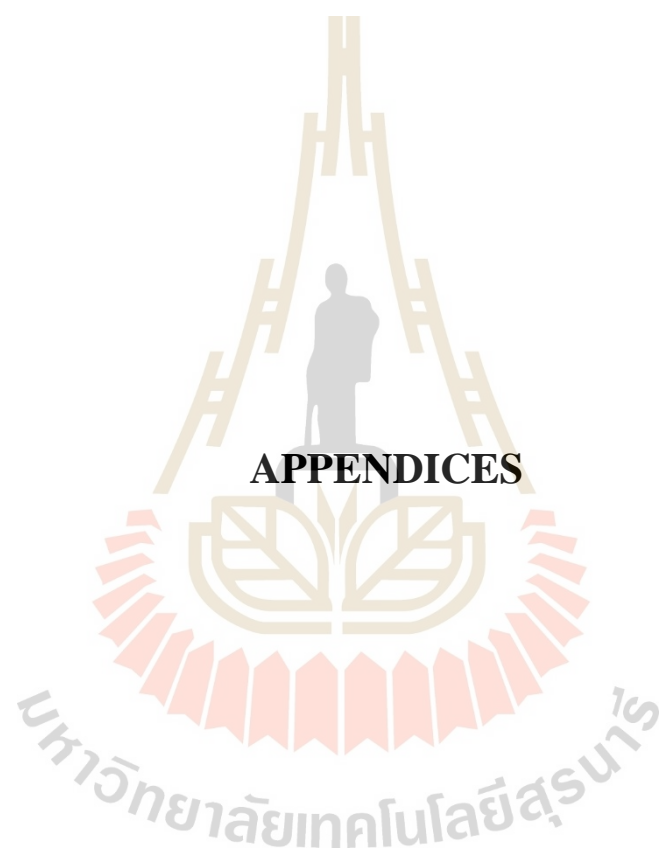
- Stengel, M. (2011). First-principles modeling of electrostatically doped perovskite systems. **Phys. Rev. Lett.** 106: 136803.
- Takesada, M., Yagi, T., Itoh, M., and Koshihara, S.-y. (2003). A gigantic photoinduced dielectric constant of quantum paraelectric perovskite oxides observed under a weak DC electric field. **J. Phys. Soc. of Jap.** 72(1): 37.
- Thiel, S., Hammerl, G., Schmehl, A., Schneider, C. W., and Mannhart, J. (2006). Tunable quasi- two- dimensional electron gases in oxide heterostructures. **Science.** 313: 1942.
- Van Benthem, K., Elsässer, C., and French, R. H. (2001). Bulk electronic structure of SrTiO₃: Experiment and theory. **J. Appl. Phys.** 90: 6156.
- Wang, Z., Zhong, Z., Hao, X., Gerhold, S., Stöger, B., Schmid, M., Sánchez-Barriga, J., Varykhalov, A., Franchini, C., Held, K., and Diebold, U. (2014). Anisotropic two-dimensional electron gas at SrTiO₃(110). **Proc. Natl. Acad. Sci. USA.** 111: 3933.
- Webb, G. W. (1969). Low-temperature electrical resistivity of pure Niobium. **Phys. Rev.** 181(3): 1127.
- Wood, J. (2007). Oxides put waste heat to work. **Materials Today.** 10(3): 15.
- Yoshimatsu, K., Yasuhara, R., Kumigashira, H., and Oshima, M. (2008). Origin of metallic states at the heterointerface between the band insulators LaAlO₃ and SrTiO₃. **Phys. Rev. Lett.** 101: 026802.
- Zhang, W. (2013). Angle-Resolved Photoemission Spectroscopy. 19-49. doi: 10.1007/978-3-642-32472-7_2.
- Zhu, Y., Shi, D. N., Du, C. L., Shi, Y. G., Ma, C. L., Gong, S. J., Zhang, K. C., and Yang, Z. Q. (2011). Half-metallic interface with stronger ferromagnetism in

(110)-oriented $\text{La}_x\text{Sr}_{1-x}\text{MnO}_3/\text{SrTiO}_3$ ultrathin superlattices. **J. Appl. Phys.** 109: 116102.

Zollner, S., Demkov, A. A., Liu, R., Fejes, P. L., Gregory, R. B., Alluri, P., Curless, J. A., Yu, Z., Ramdani, J., Droopad, R., Tiwald, T. E., Hilfiker, J. N., and Woollam, J. A. (2000). Optical properties of bulk and thin-film SrTiO_3 on Si and Pt. **Vac. Sci. Technol. B.** 18(4): 2242.

Zubko, P., Gariglio, S., Gabay, M., Ghosez, P., and Triscone, J.-M. (2011). Interface Physics in complex oxide heterostructures. **Annu. Rev. Condens. Matter Phys.** 2: 141.





APPENDICES

APPENDIX A

EXTRACTED VALUE FROM THE EXPERIMENTAL DATA

The quantitative values from our data are mostly extracted by fitting. The first thing to know is, the photoemission intensity is generally contributed by the Lorentzian and Fermi function with the specific background. However, the region near the Fermi energy could be simplified by using only the Lorentzian function. The constant momentum dispersion (MDC) and energy dispersion (EDC) from ARPES are general collectible and very useful data. Lorentzian function has general formula of

$$f(x) = y_0 + \frac{A}{(x-x_0)^2+B} \quad (\text{A.1})$$

where x_0 is the center of the peak and B is normally used to describe the full width at half maximum (FWHM). We typically use the high-order polynomial to track the lineshape of data in low-energy region. However, in high range of energy measurement like XPS, required Shirley background to obtain the good fitting. There are some important values need to be mentioned about how to take them from the ARPES. Firstly, the carrier effective masses which generally be extracted at the Fermi pocket or VBM. The carrier densities at the Fermi level which can be represented the 2D behavior of the sample surfaces.

A.1 The effective masses

The effective masses carry the information about the electron mobility by this equation

$$\mu = \frac{q}{m^*} \bar{\tau} \quad (\text{A.2})$$

where $\bar{\tau}$ is the average scattering time, the electron mobility (μ) is inverse proportional to the effective masses (m^*). This has been used to describe the quasiparticle term in electron interacting system. There are two steps to track the band dispersion in this region. Firstly, EDC at each fixed energy has to be fitted by the Lorentzian function which will give us a peak position for any constant momentum. After the single peak has been obtained from EDC, then we have to do line fit continuously over the whole regions of interest. The second step, we have to exploit the parabolic equation to fit among the peaks collected from EDCs. The band dispersion peaks (at VBM or CDM) always behaves like parabola band (in 2DEG system) which are obviously fit through the parabolic equation. The comparison between parabolic equation and nearly-free electron can be expressed as

$$y = mx^2 \text{ and } E = \frac{\hbar^2 k^2}{2m^*} \quad (\text{A.3})$$

We can see that the parabolic coefficient (m) is comparable to the nearly-free electron like ($\frac{\hbar^2}{2m^*}$). So, we can get the effective masses by fitting the data using parabolic equation. The effective masses from our LaSTO (110) have been extracted by this method. Firstly, we extract the peak of each EDCs by fitting the state with 1-3 Lorentzian curves and second-order polynomial background depended on number of bands at specific region. As shown in figure 4.2, We could observe at least 3 bands and

the Fermi wave numbers (k_F) were different in crystalline direction. In k_M -direction, we could not observe the third band for MDC measurement but we can approximate the k_F of the third band roughly $0.4-0.6 \text{ \AA}^{-1}$ for consideration the FSM (see figure 4.3(a) and (b)) which is the largest of k_F with heavy mass. The first band (the inner band of figure 4.2(a) or figure 4.2(b)) is strongly dispersion (lightly mass) but the second band is weakly dispersion (heavy mass) and the k_F of them were about 0.08 and 0.26 \AA^{-1} with have their bandwidths situated 0.054 eV and $0.068-0.126 \text{ eV}$ below E_F , respectively. In k_Z -direction, the first band (the outer band of figure 4.2(c) or figure 4.2(d)) is weakly dispersion (heavy mass), the k_F was about $0.33-0.36 \text{ \AA}^{-1}$ and its bandwidth situated 0.051 eV while the second and the third bands were the strong dispersion (lightly mass) which k_F were about $0.09-0.10$ and $0.13-0.16 \text{ \AA}^{-1}$ and their bandwidths situated 0.073 eV and 0.104 eV below E_F , respectively. The effective masses could calculate as following; a heavy ($m^* \cong (10-13)m_e$), a semi-heavy ($m^* \cong (1-2)m_e$), and a lightly ($m^* \cong 0.35m_e$), effective mass along k_z or $[001]$ -direction while a heavy ($m^* \cong (4.6-5.4)m_e$) and a lightly ($m^* \cong (0.3-0.4)m_e$) effective mass are observe along k_m or $[1\bar{1}0]$ -direction.

A.2 The density of carrier

The clean surface insulating including our samples (STO and LaSTO) which is expected to have no spectral weight at Fermi energy. Interestingly, Meevasana et al. can probe the 2DEG density (at the Fermi level) which have been developed as a function of UV irradiation doses (Meevasana et al., 2011). In our work, we focused on the saturated state by dosing more than $1,000 \text{ Jcm}^{-2}$ before starting any of the measurements. To obtain the Fermi map, we have measured the set of ARPES data over

the first two-Brilluion zone. We then do the Fermi mapping by using Igor macro which is simply connect each spectras in the function of measured angle (with specific relation). The Fermi surface map (FSM) can be obtained by choosing the Fermi energy at the final state of our spectrum. Then we fit our FSM by Lorentzian function to get all peaks at the Fermi surface. Finally, we can fit those bands by either ellipsoidal or circular equation to get the sketch of all bands in our experiment. As shown in figure 4.3, we can see at least 3 subbands at the Fermi level of our sample.

We estimate the surface charge density from the Luttinger area of these measured, two-dimensional, Fermi surface pockets at the gamma point by calculating area of all Fermi surface (can be applied to other Fermi level shapes). Here, we have 3 Fermi pocket with corresponding area of $54.42 \times 10^{14} \text{ cm}^{-2}$. Then, the corresponding 2D carrier density was calculated; $n_{2D} = A_L / 2\pi^2$ where which reach to the value of $2.34 \times 10^{14} \text{ cm}^{-2}$. This confirmed the 2DEG conducting surface and subband structure of our STO (110) sample.

APPENDIX B

CRYOSTAT SYSTEM

In this chapter, I would like to express our work on setting up the cryostat system. The aim of this work is to measure the basic physical quantities such as resistivity and magnetic property at low temperature. This section can be divided into 3 main parts; instrumental setup, sample preparation and resistivity measurement, which will be represent below.

B.1 Instrumental setup

Our instruments consist of 3 main components; an expander-model DE202, a compressor of Advanced Research Systems Inc., and a temperature controller-model 331S of Lake Shore Cryotronics Inc. (Figure B.1). These commercial setup are used for a closed-cycle cryostat system which have to cooperate to a chiller and a vacuum pump. It operates on the principle of the refrigeration cycle under the vacuum pressure better than 1×10^{-6} torr. Our real setup is shown in figure B.2. A proportional-integral-derivative (PID) was used for controlling the temperature in this system in the range between 5 and 350 K.

For setting this system, we connected the compressor to the chiller by two ports of cooling water and connected to the expander by two gas lines and an electrical power cable. One of gas lines supplies the high pressure of helium gas to the expander, the other gas line returns low pressure helium gas from the expander back to the compressor. The expander electrical power from the compressor drives the valve of

motor which is inside the expander and the vacuum pump was connected to the pump out port of the expander. The temperature controller connects to the instrumentation port of the expander. The simple diagram is shown in figure B.3.



Figure B.1 The cryostat system including an expander, a compressor and a temperature controller.

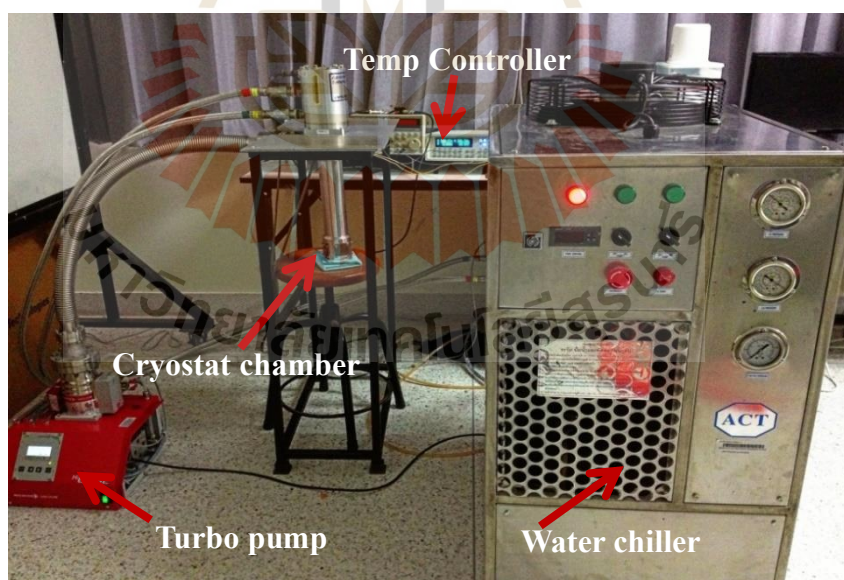


Figure B.2 Real setup of our cryostat system consisting of; cryostat chamber, temperature controller, turbo pump, and water chiller.

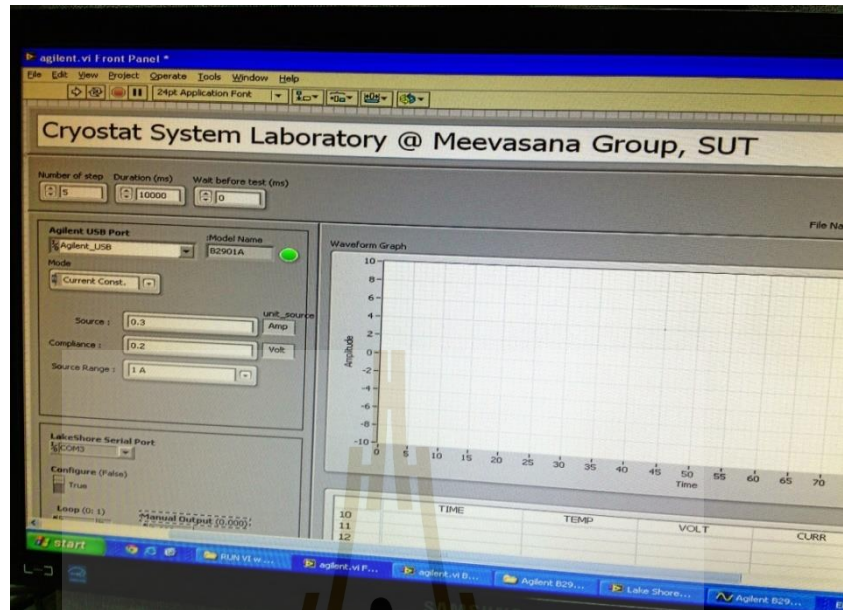


Figure B.4 Prototype of LabVIEW front panel using to measure resistance in our cryostat setup.

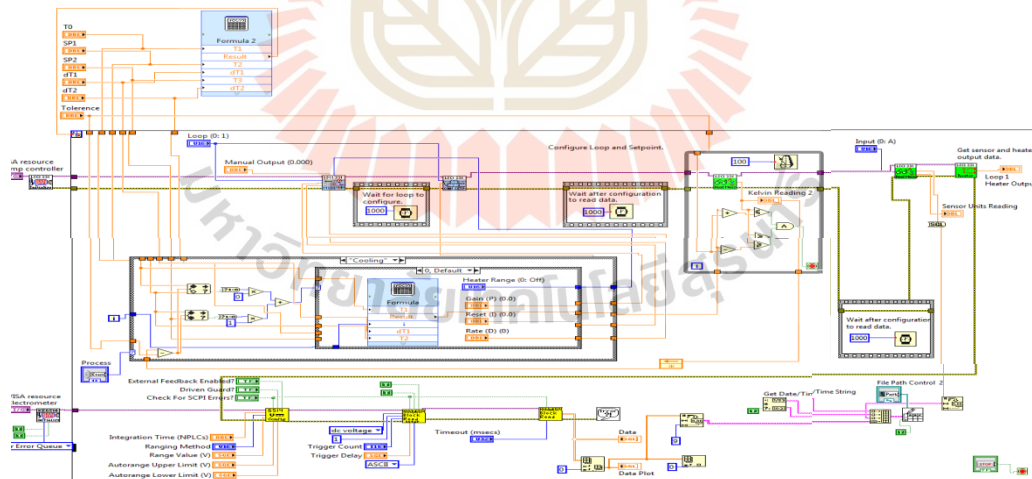


Figure B.5 Block diagram for controlling the operation of system.

B.2.2 Sample preparation for testing and calibration

Niobium (Nb) was used for a temperature calibration by measurement the resistivity and look for the superconducting transition. It was flat and cut into the dimension of $2 \times 3 \times 7 \text{ mm}^3$ roughly, cleaned the surface and stick on the sapphire substrate with conductive epoxy. After that it was made the Ohmic contact by using a spot welding and a soldering method (see figure B.6).

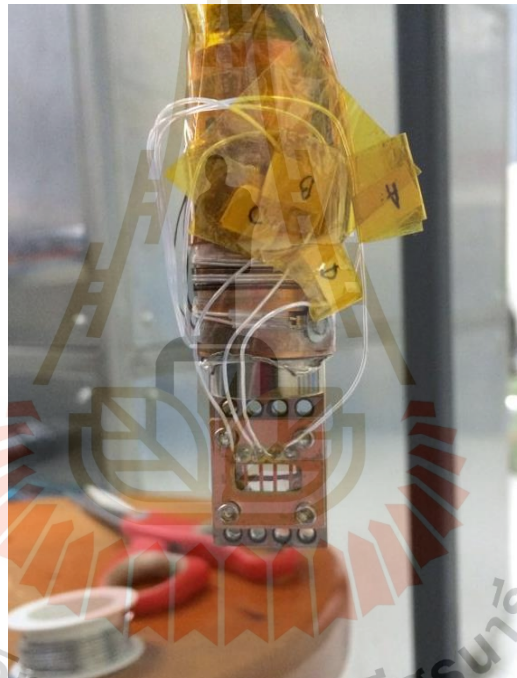


Figure B.6 Sample preparation, sample were mounted with the sample holder by spotted welding and wired with silver wire. The silver wire will be connected to the electrical port to make an electrode for 4-point probe measurement.

B.3 Procedures of electrical measurement

B.3.1 Resistivity measurement and four-point probe method

The common techniques for the resistance measurement are the two-point probes and four-point probes method as shown the diagram in figure B.7. The two-point probe method gives a value with contributions from contact wires, contact resistance and hence not advisable in the case of metals where the sample resistance is very low. The four-point probe method minimizes the other contributions (lead resistance, contact resistance, etc.) to the resistance measurement which results in an accurate measurement of sample resistance (Smits, 1957).

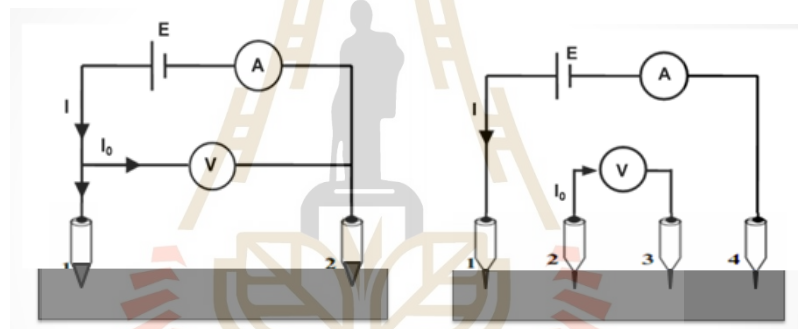


Figure B.7 Diagram of two- and four-point probe method.

In this work, we prepared the sample for the four-point probe (FPP) method. The outer probes were used for sourcing the current with connect to a power supply and the two inner probes were connected to electrometer (model: Keithley-6514) for measuring the resulting voltage drop across the surface of the sample. The precise resistance of the sample can be determined by the Ohm's law, which is calculated by dividing the voltage drop across it by this current. However, we can also use the two-probe method for high resistance samples.

B.3.2 Resistivity measurement for temperature calibration

We measured the temperature dependence of the voltage (constant current) of the Nb metal and found the superconducting state at around 9.4 K in cooling process (see figure B.8). The phase transition of Nb metal from metallic to superconductivity are well known at the critical temperature, $T_c = 9.2$ K (Wzsat, 1969). Therefore, this indicates that our setup may have the temperature mismatch about 3.4 K which may be caused by the bad electrical contact or sample environment. We hope our system can be further improved by our new calibration.

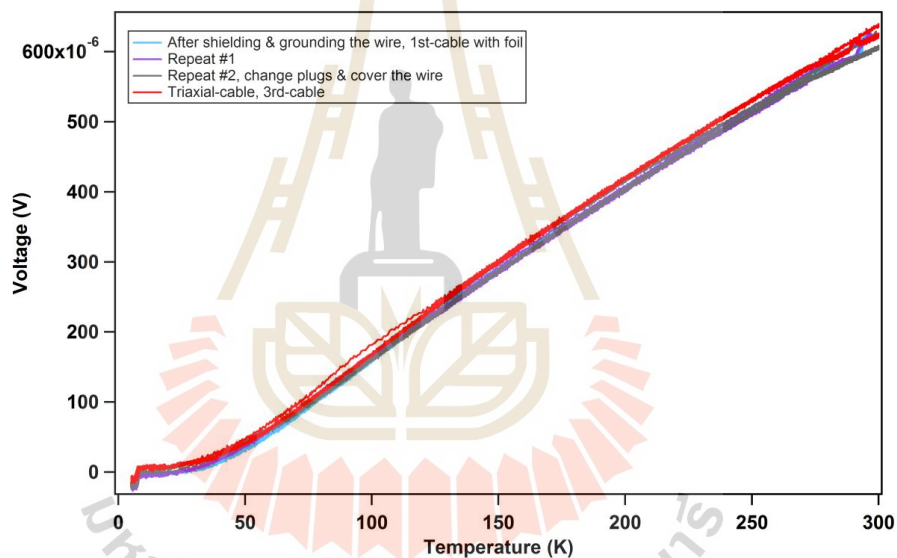


Figure B.8 Temperature dependence of the measured voltage (constant current) of Nb metal showing the transition from metallic to superconducting phase at 9.4 K.

CURRICULUM VITAE

NAME Mrs. Pornpana Buaphet

DATE OF BIRTH September 12, 1976

PLACE OF BIRTH Nakhon Si Thammarat

PLACE OF WORK Physics department, Faculty of Science,
Thaksin University, Phattalung, 93210

PERSONAL ADDRESS 45 Moo2, Thayang, Thungyai District,
Nakhon Si Thammarat 80240, Thailand
Mobile. 66-88-5957564

E-MAIL pornpanabuaphet@gmail.com

EDUCATIONS

2011 - 2015 Suranaree University of Technology,
Nakhon Ratchasima, Thailand.
Doctor of Philosophy (Physics)